Energy &
Environmental
Science

ROYAL SOCIETY
OF CHEMISTRY

REVIEW

View Article Online
View Journal | View Issue

Cite this: *Energy Environ. Sci.*, 2025, **18**, 5159

Advances in hexaazatriphenylene-based COFs for rechargeable batteries: from structural design to electrochemical performance

Zhonghui Sun,[a] Zhongping Li,*[bc] Jinsong Peng,[a] Xiaomeng Yan,[a] Hang Shang,[a] Yucheng Jin,[c] Qiannan Zhao,[c] Changqing Li,*[c] Siliu Lyu,[c] Chunxia Chen*[a] and Jong-Beom Baek *[c]

Received 21st March 2025,
Accepted 28th April 2025

DOI: 10.1039/d5ee01599e

rsc.li/ees

As commercial batteries reach capacity and energy density limits, especially with graphite anodes and transition metal cathodes, the need for advanced alternatives grows. Organic electrodes offer the promise of high capacity, sustainability, and tunable structures. Among them, hexaazatriphenylene (HATP)-based covalent organic frameworks (COFs) have gained considerable attention because of their distinctive characteristics. HATP-based COFs are formed with an electronegative skeleton within one-dimensional channels, and exhibit a strong affinity for metal ions (Li^+, Na^+, K^+, Zn^{2+}). Their distinct structure significantly enhances both ion transport and reaction kinetics. Moreover, HATP-based COFs exhibit highly ordered, permanent porosity and large surface areas, while their dense active sites and tunable conductivity facilitate rapid redox processes and enhanced capacity, leading to improved electrochemical performance. Additionally, their conjugated nature ensures robust physical and chemical stability, minimizing side reactions and maintaining structural integrity and cycling stability. As a result, HATP-based COFs are particularly well-suited for various rechargeable batteries, including lithium-ion, sodium-ion, potassium-ion, and aqueous zinc-ion batteries. This review explores the development and design principles of HATP-based COFs, analyzes their electrochemical performance and redox mechanisms, and addresses the challenges and future directions for their application in energy storage technologies.

Broader context

In the current era of ubiquitous interconnectivity, demand for high-energy-density rechargeable batteries with superior electrochemical reliability continues to rise. Organic electrode materials have emerged as compelling alternatives to conventional inorganic counterparts, in part because they offer tunable molecular structures, environmental sustainability, and high theoretical capacity. Among them, hexaazatriphenylene-based covalent organic frameworks (HATP-based COFs) have been increasingly explored because of their reversible electrochemical redox activity, high theoretical specific capacities, and tunable electronic conductivity enabled by molecular design. Their electronegative skeletons confined within one-dimensional channels, coupled with exceptional structural stability, further enhance their potential for next-generation energy storage applications. This review provides a comprehensive analysis of HATP-based COFs as electrode materials for rechargeable batteries, including lithium-ion, sodium-ion, potassium-ion, and aqueous zinc-ion systems. It delves into their structural design principles, synthetic methodologies, and strategies for optimizing redox-active sites and morphological characteristics. The review further elucidates the underlying electrochemical mechanisms, emphasizing the correlation between molecular structure, charge transport dynamics, and ion diffusion kinetics. Additionally, it highlights recent advancements, persistent challenges, and key approaches for enhancing the stability, conductivity, and overall energy efficiency of HATP-based COFs. Finally, it presents prospective modification strategies and outlines future research directions for their development for high-performance rechargeable battery technologies.

1. Introduction

The growing demand for efficient and sustainable energy storage solutions has accelerated the development of high-performance rechargeable secondary batteries capable of storing and releasing energy multiple times.[1–3] Rechargeable batteries are increasingly utilized in applications such as electric vehicles, smart grids, and large-scale power systems.[4–6] However, the conventional electrode

---

[a] *College of Chemistry, Chemical Engineering and Resource Utilization, and Center for Innovative Research in Synthetic Chemistry and Resource Utilization, Northeast Forestry University, Harbin 150040, P. R. China. E-mail: ccx0109@nefu.edu.cn*

[b] *Key Laboratory of Automobile Materials of MOE and School of Materials Science and Engineering, Jilin University, Changchun 130012, P. R. China. E-mail: lizhongping2025@jlu.edu.cn*

[c] *Department of Energy and Chemical Engineering/Center for Dimension-Controllable Organic Frameworks, Ulsan Nation Institute of Science and Technology (UNIST), Ulsan 44919, Republic of Korea. E-mail: lizhongping2023@unist.ac.kr, changqingli@unist.ac.kr, jbbaek@unist.ac.kr*

materials used in rechargeable batteries, such as graphite for the anode and transition metal-based compounds for the cathode, are reaching their limits in terms of capacity and energy density (150–250 W h kg^{-1}).[7,8] The size and valence of the counterions need to be matched to the crystal inorganic structure due to lattice and structural stability limitations, inherently reducing the versatility as high-performance electrodes in lithium-ion batteries (LIBs) that often prove incompatible with other metal-ion systems.[9,10] Additionally, the scarcity and toxicity of transition metal resources not only constrain the mass production to meet rapidly growing demands, but also complicate recycling processes and exacerbate environmental pollution.[11,12] These factors have driven ongoing efforts to develop alternative rechargeable battery technologies with improved cost-effectiveness, safety, and sustainability, especially for large-scale applications.[13]

Organic materials capable of reversible electrochemical redox reactions offer several advantages over traditional inorganic materials. They include higher theoretical specific capacities, adjustable voltage platforms through molecular design, and environmental benefits because of the absence of heavy metals.[14–16] Organic materials composed of light elements such as like carbon (C), hydrogen (H), oxygen (O), nitrogen (N), and sulfur (S), and especially those containing electronegative elements, can effectively interact with a wide range of metal-ions (*e.g.*, Li^+, Na^+, K^+, Mg^{2+}, Al^{3+}, Zn^{2+}), making them suitable for various secondary batteries.[17–19] Additionally, organic materials are cost-effective, readily available, and possess soft mechanical properties, making them ideal for flexible batteries.[20,21] However, traditional organic electrode materials have challenges, such as the dissolution of active materials during cycling, low conductivity, and the limited accessibility of redox-active sites.[22] To overcome these limitations, a deeper understanding of fundamental properties, mechanisms, and structure–performance relationships is urgent and essential.

Covalent organic frameworks (COFs) have emerged as a promising class of crystalline materials linked by robust covalent bonds, resulting in highly stable conjugated π-skeletons.[23–35] COFs can be synthesized with diverse topologies, skeletons, and pore structures due to a diverse range of topological design diagrams, the availability of building units, and the accessibility of linkages.[36–40] One of the most significant features of COFs is the ability to pre-design their functional structures *via* topological diagrams, which enables materials to be created with well-defined wall interfaces.[41–45] The unique properties of COFs—including permanent and adjustable porosity, large surface area, excellent thermal and chemical stability, and tailored structural designability—make them highly attractive for a wide range of applications, including gas adsorption/separation, photo/electro-catalysis, chemical detection, and energy storage.[46–58]

Redox-active anchored COFs were first employed in 2015 as electrode materials in lithium-ion batteries (LIBs), demonstrating their ability to undergo reversible redox reactions.[59] Since then, COFs with various structural motifs including benzoquinone, imide, azo, pyrazine, imidazole, phenazine, anthraquinone, and so on, have been explored for use in LIBs, sodium-ion batteries (SIBs),[60,61] potassium-ion batteries (KIBs),[62,63] and aqueous zinc-ion batteries (AZIBs),[64–66] these COFs offer highly ordered skeletons, large surface area, adjustable conductivity, and excellent solvent resistance.

Among them, hexaazatriphenylene (HATP)-based COFs have attracted significant attention due to their unique structural and functional properties (Fig. 1(a)). These COFs feature an electronegative skeleton within well-defined one-dimensional (1D) channels, and exhibit strong metal cation affinity (Li^+, Na^+, K^+, and Zn^{2+}), which enhances both ion transport and transport kinetics.[67,68] Moreover, the exceptionally designable structure permits HATP-based COFs with precisely ordered permanent porosity, large surface areas, and adjustable conductivity, synergistically enabling accelerated redox reactions. Their highly π-conjugated structure not only ensures excellent physical and chemical stability but also facilitates the electron transfer processes, contributing to the longevity and fast charge efficiency of electrodes.[69] Furthermore, the planar structure enables efficient π–π stacking interactions, further strengthening both solvent resistance and chemical degradation tolerance, even under prolonged cycling.[70] The dense C═N bonds serve as redox-active sites capable of undergoing a reversible 6-electron transfer process, giving the COFs an impressive theoretical capacity.[71] The combination of these characteristics—excellent stability, tunable conductivity, high capacity, and fast cation transfer—make the HATP-based COFs highly promising as materials for next-generation electrode applications.

Not surprisingly, increasing demand for sustainable, high-performance electrode materials has sparked significant interest in HATP-based COFs for rechargeable batteries over the past decade (Fig. 1). This review provides a comprehensive overview of their key research development, identify ongoing challenges, and explores innovative strategies for structural optimization and performance enhancement. It delves into various synthesis strategies and highlights how structural and functional modifications influence their electrochemical properties. Special attention has been given to the unique advantages and engineering of the redox mechanisms of HATP-based COF electrodes in LIBs, specifically addressing challenges such as insufficient and buried redox-active sites and limited electron transport, while also exploring potential solutions to overcome these limitations. Additionally, the review covers the applications of HATP-based COFs in SIBs, PIBs, and AZIBs, demonstrating the versatility of these materials across different types of energy storage systems. Finally, future research directions are outlined, focusing on the structural diversification of COFs, enhancement of their conductivity, regulation of morphology, development of scalable production methods, and optimization of advanced characterization methods. These insights are intended to guide the continued progress of HATP-based COFs, contributing to next-generation, sustainable energy storage technologies.

2. Synthesis strategy of HATP-based COFs

HATP-based COFs are synthesized through two primary strategies: direct one-step synthesis and indirect multi-step approaches (Fig. 2).

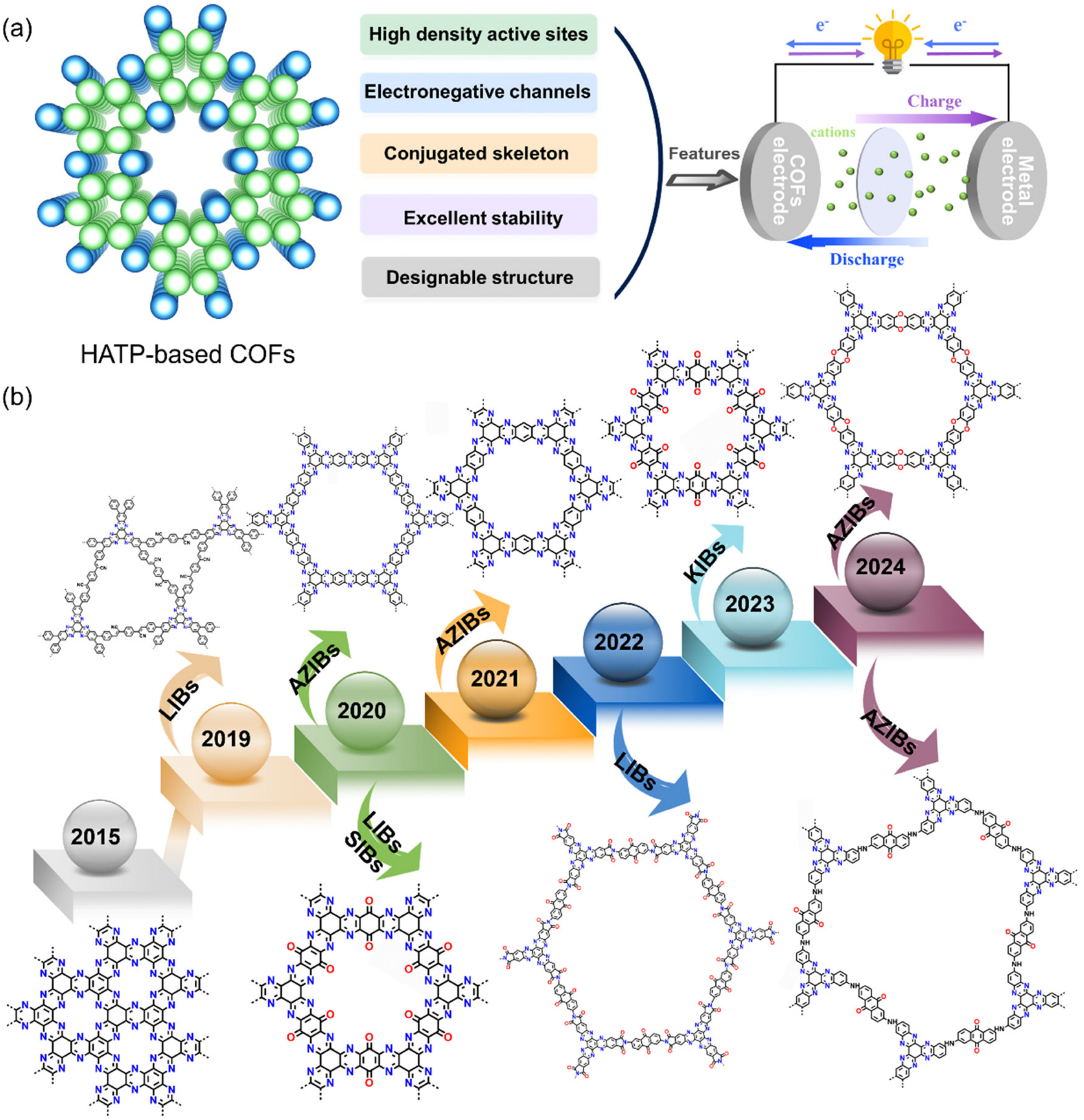

Fig. 1 (a) Schematic representation of the key features of HATP-based COFs in rechargeable batteries. (b) Timeline of key developments in HATP-based COF electrodes for rechargeable batteries.

The direct one-step synthesis involves the straightforward polymerization of cyclohexanehexone octahydrate (CHHO) with polyamine compounds,[72–74] which is highly efficient. However, this method has difficultly precisely controlling connectivity and incorporating functional groups. In contrast, the indirect synthesis approach begins with the preparation of small molecules with functional groups capable of forming various dynamic covalent linkages, such as imine,[75,76] imide,[77] phenylimino,[78] and triazine.[79] This strategy enables superior control over the molecular structure, stability, and functionality of the COFs, offering greater flexibility and versatility when designing COFs with tailored properties for specific applications.

2.1 The direct one-step synthesis method

The direct one-step solvothermal synthesis of HATP-based COFs relies on the condensation reaction between CHHO and organic amines (tetramines, hexamines, and octamines), an efficient and straightforward approach for constructing highly symmetrical and rigid COF structures. This method is advantageous due to its simplicity, requiring only appropriate solvent selection and temperature control to promote imine bond formation without the need for expensive catalysts. The reaction mixture underwent flash frozen in a liquid nitrogen bath and evacuated under vacuum for three pump–thaw cycles, ensuring complete degassing and oxygen removal prior to hydrothermal reaction. Furthermore, the crystallinity and electrochemical performance of HATP-based COFs could be significantly enhanced through optimizing the catalyst systems (potassium hydroxide (KOH) or various acid systems) and reaction conditions. These optimizations achieved exceptional crystallinity, structural regularity, high surface areas and tunable conductivity, thereby providing efficient ion transport and electron transfer for high-performance electrodes.

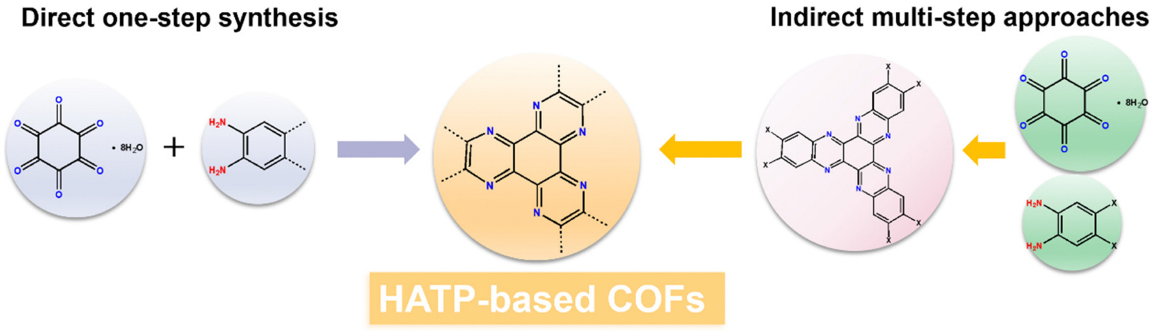

Fig. 2 Schematic diagram of the synthesis method for HATP-based COFs.

The selection of amines precursors also plays a pivotal role to determine the electrochemical performance of HATP-based COFs (Fig. 3). Redox-active amines, including 2,3,5,6-tetraminobenzoquinone (TABQ) and 2,3,7,8-tetraaminophenazine-1,4,6,9-tetraone (TAPT), incorporate additional redox-active $C{=}N$ and $C{=}O$ groups to HATP-based COFs that enable multi-electron redox reactions, elevating the theoretical capacities. Three-dimensional (3D) amines endowed HATP-based COFs with hierarchical porosity and enhanced surface areas, which synergistically optimized ion diffusion kinetics while ensuring accessibility of redox-active sites, collectively enabling high reversible capacity. Alternatively, non-redox-active two-dimensional (2D) amines promoted the construction of extended π-conjugation skeletons that exhibited enhanced charge transport properties and cycling stability, attributing to their improved electronic delocalization and dissolution resistance to electrolyte dissolution.

In 2015, Baek's group pioneered this approach by synthesizing the first HATP-based COF, C_2N-h_2D crystal, through the condensation of hexaaminobenzene trihydrochloride and CHHO in *N*-methyl-2-pyrrolidone (NMP) with a few drops of sulphuric acid (H_2SO_4) or trifluoromethanesulphonic acid at 175 °C for 8 h (Fig. 4(a)).[80] The scanning tunnelling microscopy (STM) results confirmed formation of a well-defined layered network featuring uniformly distributed nitrogen atoms within its porous structure (Fig. 4(b)). The measured inter-hole distance was 8.24 ± 0.96 Å obtained from the height profiles, agrees well with the theoretical value (Fig. 4(c)). Additionally, to fabricate large-area films, the as-synthesized C_2N-h_2D crystals were dispersed in trifluoromethanesulfonic acid and drop-cast onto the preheated (140 °C) SiO_2/Si substrate, followed by high-temperature annealing at 700 °C under argon for 2 h. The solution-casted films were then transferred onto flexible polyethylene terephthalate substrates *via* poly(methylmethaacrylate)-mediated processes. Atomic force microscopy (AFM) characterization of the C_2N-h_2D crystal flakes demonstrated an average thickness of 8.0 ± 3.5 nm, confirming the formation of multilayer stacks (Fig. 4(d)). Furthermore, the shiny metallic reflection observed in the C_2N-h_2D film indicated a high degree of crystallinity (Fig. 4(e) and (f)). Compared to graphite, C_2N-h_2D exhibited a reduced interlayer distance and stronger interlayer interactions, leading to improved semiconducting behavior and excellent electrical properties.

The designed amine precursors played a crucial role in tailoring pore structure properties, facilitating the creation of COFs for diverse applications. Inspired by this breakthrough, a uniformly microporous, robust 3D cage-like organic network (CON) structure was synthesized by condensing triptycene-based hexamine with CHHO in an ethylene glycol/acetic acid mixture at 130 °C for 80 h.[74] The resulting 3D-CON exhibited a remarkably high Brunauer–Emmett–Teller (BET) surface area of 2247 $m^2\ g^{-1}$ and a uniform pore size distribution of 0.55 nm, attributed to its periodic microporous structure and multi-dimensional connectivity. This work confirmed that HATP-based 3D network structures constructed with steric hexamines and octaamines were superior to traditional 2D frameworks in terms of surface area, porosity, and functional versatility. The combination of high surface area and rigid skeleton enabled fast and stable electrolyte infiltration and cation transport, making this material a promising candidate for high-performance energy storage applications.

Since these pioneering developments, HATP-based COFs have been continuously improved, with ongoing research focused on fine-tuning the reaction conditions to enhance crystallinity and functional properties. Mirica *et al.* synthesized fused π-conjugated aza-COF-1 and aza-COF-2 by condensing CHHO and 2,3,6,7,10,11-hexaaminotriphenylene hexahydrochloride and 1,2,4,5-benzenetetramine tetrahydrochloride (BTA·4HCl), respectively.[81] After 5 days of reaction at 185 °C, well-ordered crystalline frameworks were achieved in the presence of concentrated H_2SO_4 as a catalyst. Powder X-ray diffraction (PXRD) patterns revealed distinct crystalline features: aza-COF-1 exhibited sharp peaks at 7.78, 13.44, and 26.67° corresponding to the (100), (110), and (001) planes of a layered structure, whereas aza-COF-2 showed broader peaks at 6.51 and 26.51° assigned to the (100) and (001) planes, respectively. Both COFs exhibited superior proton conductivity values at $10^{-3}\ S\ m^{-1}$, leading to the development of stable and high proton-conductive materials. Chou *et al.* synthesized CPT by the condensation reaction of CHHO with redox-active 2,3,7,8-phenazinetetramine (PT) under an acetic acid-catalyzed condensation reaction at 150 °C for 4 days, which exhibited rich electron delocalization, needle-like morphology and thinner sheet thickness.[82] The high intrinsic conductivity ($1.58 \times 10^{-1}\ S\ m^{-1}$) coupled with abundant redox-active sites enabled it a proper electrode material for high-performance energy storage systems. The optimized

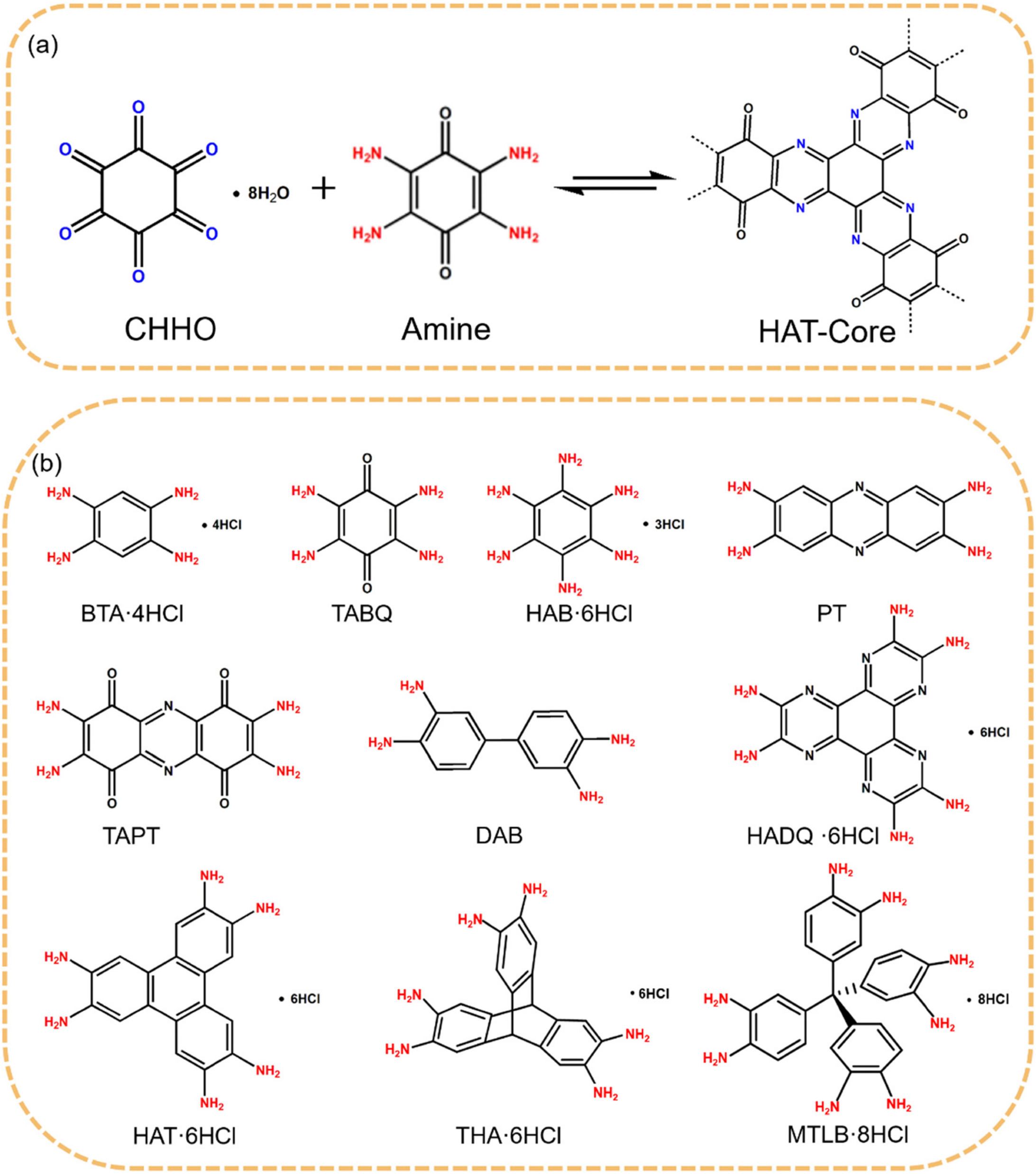

Fig. 3 (a) Schematic illustration of the direct one-step method. (b) Various reported amines precursors utilized in the synthesis of HATP-based COFs.

reaction conditions led to better crystalline COFs, which was important, to ensure uniform pore size distribution and improve the electrochemical performance of the electrode materials and supercapacitors.

The choice of catalyst has a crucial effect on the crystallinity and structural regularity of HATP-based COFs, which in turn significantly affects their electrochemical performance. Liu *et al.* focused on the condensation between BTA·4HCl and CHHO to synthesize highly crystalline PGF-1, which was obtained in 4 M aqueous KOH solution at 120 °C in a sealed vessel after 3 days (Fig. 5(a)).[83] The PXRD pattern of the PGF-1 revealed two prominent peaks at 6.1° and 26.4°, which corresponded to the (100) and (001) planes, respectively (Fig. 5(b)). These PXRD features were matched well with the simulated AA eclipse stacking structure and the corresponding predicted pore size was 1.2 nm, consistent with the experimental values derived from the adsorption isotherm (Fig. 5(c)). The high-resolution transmission electron microscopy (HR-TEM) of PGF-1 further strongly supported its high crystallinity and ordered hexagonal micropores (Fig. 5(d) and (e)). The nitrogen-rich and fully fused π-conjugated aromatic framework of PGF-1 demonstrated remarkable electrical conductivity of 3×10^{-3} S m^{-1}. In contrast, the amorphous polymer AP-1, synthesized utilizing the acid catalyst, only exhibited a broad and weak peak within the (100) region in its PXRD pattern. PGF-1, with an improved structural regularity and electronic conductivity, enabled more accessible redox-active sites and faster charge transport, resulting in higher capacity and excellent rate performance when used as the electrode material.

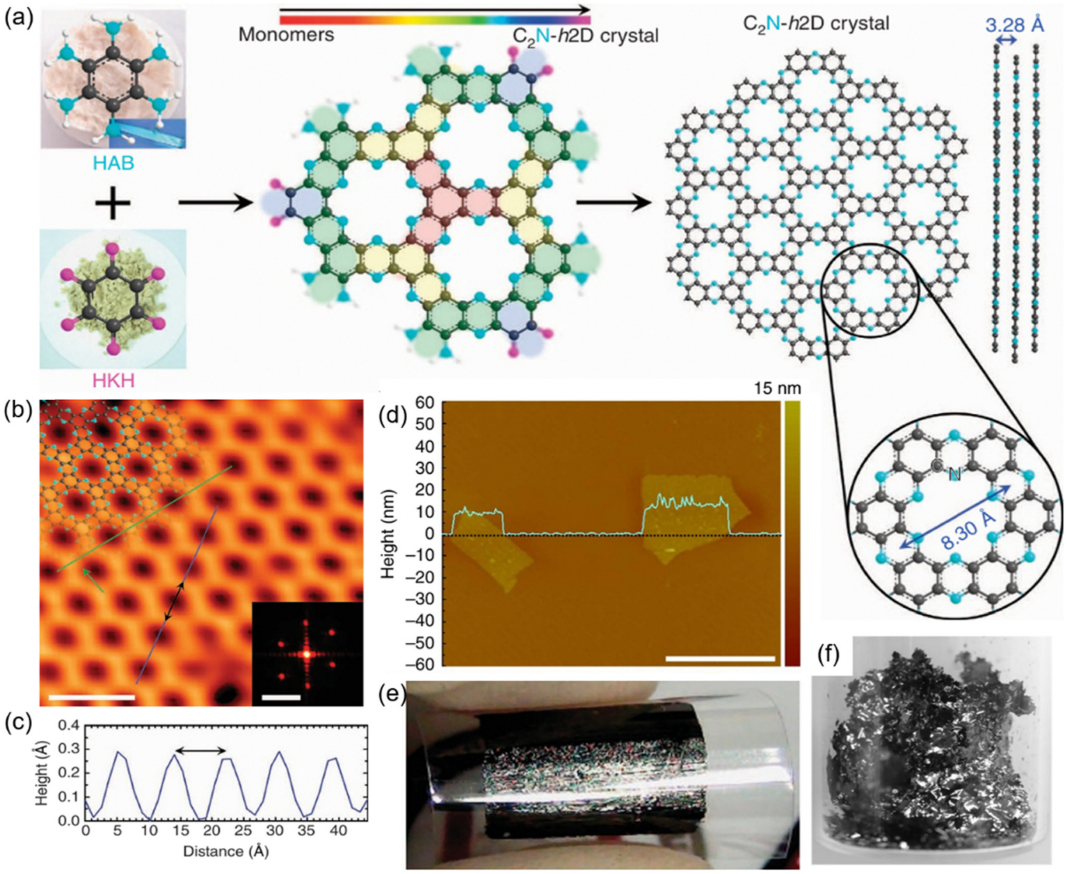

Fig. 4 (a) Synthetic route for the preparation of C_2N-h_2D. (b) Atomic-resolution STM topography image of C_2N-h_2D. (c) The topographic height profile along deep-blue line. (d) AFM image of the C_2N-h_2D crystal flakes. (e) Crystal film of C_2N-h_2D transferred onto a PET substrate. (f) Digital photograph of solution-cast C_2N-h_2D on a SiO_2 surface after heat-treatment at 700 °C. Reproduced with permission.[80] Copyright 2015, Springer Nature.

2.2 The indirect synthesis methods

The indirect synthesis of HATP-based COFs typically involves a more intricate multi-step approach, which also provides enhanced control over the molecular architecture and functionality of the final COFs. Unlike the one-step direct synthesis, which generally relies on condensation reactions between CHHO and di-amino building blocks, the indirect synthesis methods involve additional steps to prepare the precursor materials before polymerization. This method typically begins with the functionalization of HATP and hexaazatrinaphthalene (HATN)-based building blocks, which can be modified by introducing different functional groups such as amino groups ($-NH_2$),[84] cyano groups (–CN),[85,86] anhydride.[87] After functionalizing the HATP derivatives, covalent bonds are used to assemble them into the designable COF structures, utilizing different reaction types based on the intended topology, functionality, and properties of the final COFs. Prevalent polymerization strategies employed in the construction of HATP-based COFs encompass Schiff base reactions, Knoevenagel reactions, and polyimide formation. These approaches enable the synthesis of the corresponding dynamic covalent structures (Fig. 6).

2.2.1 Imine-linked HATP-based COFs. Imine-linked HATP-based COFs represent a fundamental and highly versatile class of materials, synthesized through the Schiff base condensation reaction between amines and carbonyl groups, which facilitates the formation of imine (C=N) bonds. This reaction not only underpins the creation of these materials but also lays the foundation for a wide array of structural and functional variations, making imine-linked HATP-based COFs an indispensable platform for the design of advanced electrode materials in next-generation rechargeable batteries. A significant contribution to the development of imine-linked HATP-based COFs was made by Zhao *et al.* through their indirect synthesis approach.[75] By condensing HAT-6NH_2 with terephthalaldehyde (TA) in a mixture of *N*,*N*-dimethylacetamide (DMAc), 1,3,5-trimethylbenzene and acetic acid at 120 °C for 3 days, HAT-COF was constructed with an eclipsed packing model with two triangular micropores of distinct sizes (11.3 and 15.2 Å). This unique topology provides the COF pores with distinct chemical environments: the larger pores contain aromatic C=N groups from the HATP cores, while the smaller centers share only peripheral C=N groups.

However, the BET surface area of HAT-COF was relatively low (486.15 $m^2\ g^{-1}$) due to the twisted conformation of the phenyl units in HAT-6NH_2, which distorts the framework and disrupts the ideal stacking of the COF layers. Building on this pioneering work, Zhao's group further extended their research by polymerizing HAT-6NH_2 with two other aldehyde compounds, 4,4′,4″-nitrilotribenzaldehyde (NTBA) and 4′,4‴,4′′′′′-nitrilotris(([1,1′-

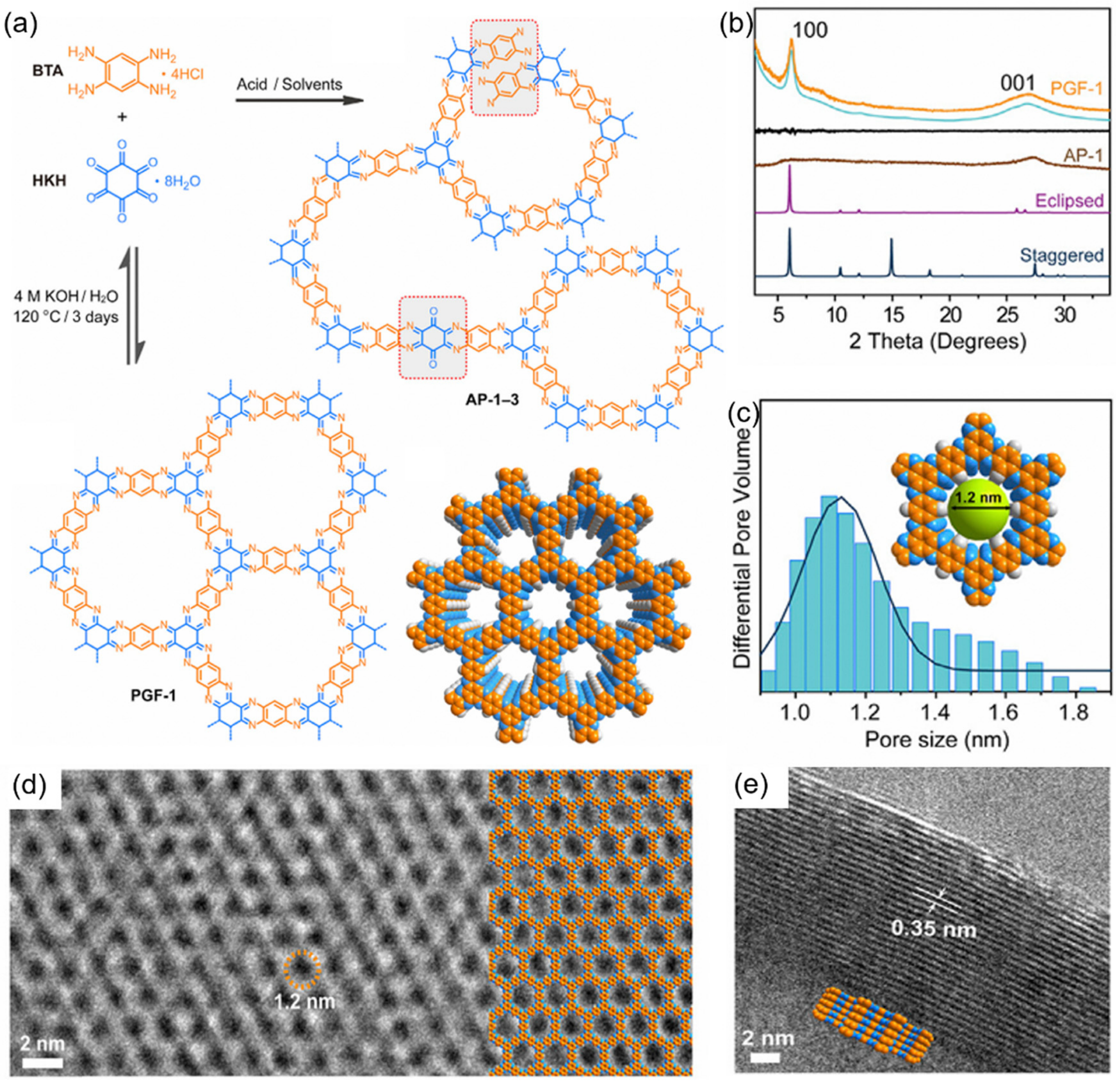

Fig. 5 (a) Synthetic route for the preparation of PGF-1 and AP-1. (b) PXRD patterns of PGF-1 and AP-1. (c) Pore size distribution profile of PGF-1. (d) and (e) HR-TEM images of PGF-1. Reproduced with permission.[83] Copyright 2020, Elsevier.

biphenyl]-4-carbaldehyde)) (NTBCA), to synthesize two new HATP-based COFs, HAT-NTBA-COF and HAT-NTBCA-COF, which both exhibited an AA stacking model (Fig. 7).[88] A distinctive feature of these COFs is the heterodromous orientation of the imine bonds, which alternate between clockwise and counterclockwise, and promote consistent bond formation between the building blocks. The specific surface areas of HAT-NTBA-COF and HAT-NTBCA-COF were 628.0 $m^2\ g^{-1}$ and 439.9 $m^2\ g^{-1}$, respectively. The pore sizes of HAT-NTBA-COF and HAT-NTBCA-COF were primarily distributed around 9.5 Å and 12.7 Å, respectively, which were consistent with the theoretical simulations (Fig. 7(c)–(g)). This variable orientation was crucial to achieving high crystallinity, and laid the ground work for the future development of multifunctional COF materials.

In addition to constructing imine-linked COFs using HATP-based amino compounds, Feng *et al.* explored a different strategy for building 2D dual-porous COFs utilizing 2,3,8,9,14,15-hexa(4-formylphenyl)diquinoxalino[2,3-*a*:2′,3′-*c*]phenazine (HATN-6CHO) and 1,4-diaminobenzene (PDA)[89] and benzidine (BZD),[90] to form 2D imine-based HATN and HATN-BZD, respectively. The reactions were carried out in a mixture of DMAc, mesitylene and acetic acid (aq. 6 M) at 120 °C for 3 days, which contributed to the high crystallinity. The larger BZD molecule, in contrast to PDA, led to larger pore size distributions of 1.0–1.3 nm and 1.8–2.0 nm. Jiang *et al.* synthesized crystalline USTB-6 by the condensation reaction of HATN-6CHO with redox-active carbonyl-rich 2,7-diaminopyrene-4,5,9,10-tetraone (PTO-NH_2), utilizing a mixed system containing DMAc, mesitylene, acetic acid (aq. 6 M) and *p*-toluidine.[76] USTB-6 exhibited a specific surface area of 328 $m^2\ g^{-1}$ with an AA stacking mode and a dual-pore structure comprising 0.7 and 1.3 nm pores. The well-defined porous structures and a high theoretical capacity of 272 mA h g^{-1} made it a suitable material for energy storage electrodes.

The above content describes the polymerization of monoamine or monoaldehyde groups with a HATP center; additionally, imine bonds and pyrazine rings can be generated between *ortho*-

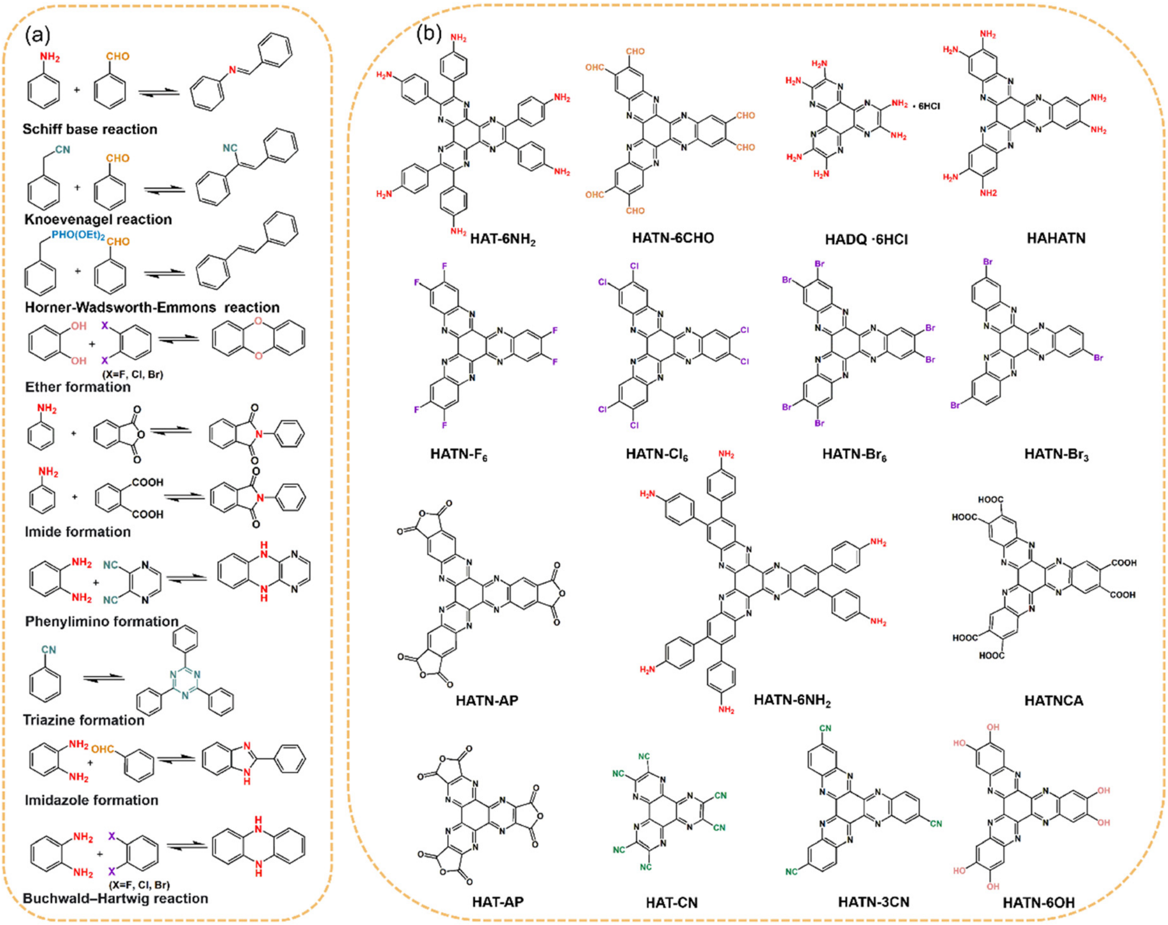

Fig. 6 (a) Representative reactions involved in the indirect synthesis methods. (b) Structure of the precursor monomer for HATP-based COFs.

diamine and *ortho*-dicarbonyl groups. Specifically, Saleem *et al.* synthesized HADQ-COF by reacting 2,3,6,7,10,11-hexaamine dipyrazino quinoxaline hexahydrochloride (HADQ·6HCl) hexahydrochloride with CHHO in the mixture of NMP and H_2SO_4 at 150 °C for 7 days, followed by a heat treatment process at 250 °C to further enhance the material's properties.[91] The thermal treatment removed edge groups and facilitated the formation of larger crystalline segments, in as confirmed by PXRD and HR-TEM observations. The enhanced crystallinity, surface area, and stability of 250-HADQ-COF made it a promising candidate for double-layer supercapacitors. Similarly, Zhu *et al.* utilized polymerization between hexaiminohexaazatrinaphthalene (HAHATN) and pyrene-4,5,9,10-tetrone (PTO) to create a 2D porous honeycomb-shaped material, which effectively improved utilization of the redox-active sites and facilitated ion transport.[69] The extended π-electron delocalization within the framework reduced both the lowest unoccupied molecular orbital (LUMO) and bandgap, demonstrating enhanced redox potential and superior electronic conductivity. The structural diversity of imine-linked HATP-based COFs offers extensive potential for the creation of highly efficient, tailored electrode materials with enhanced electrochemical performance, which are poised to drive advances in energy storage technologies.

2.2.2 Olefin-linked HATP-based COFs.

Olefin-linked HATP-based COFs represent an emerging class of materials that integrate the exceptional electronic properties of a HATP center with sp^2 hybridized carbon frameworks.[92] The reactions still required three rigorous freeze–pump–thaw cycles for thorough degassing prior to the base-catalyzed condensation reactions. Notably, recent studies demonstrated that a gradient heating strategy could significantly enhanced crystallinity.[93] The superior robust covalent architecture and extended planar π-conjugation endow them with remarkable chemical resilience and prolonged cycling stability, making them promising candidates for next-generation electrode materials.

Based on these distinct features, Feng *et al.* initially investigated olefin-linked conjugated polymers to enhance electrochemical performance while constructing electron donor–acceptor structures (Fig. 8(a)). By condensing the precursor HATN-6CHO with 1,4-phenylenediacetonitrile, 2,2′-(biphenyl-4,4′-diyl)diacetonitrile (BDAN), and 2,2′-([2,2′-bithiophene]-5,5′-diyl)diacetonitrile (ThDAN) *via* Knoevenagel condensation in a mixture of DMAc, *ortho*-dichlorobenzene (*o*-DCB) and NEt_4OH at 150 °C for 3 days, a series of olefin-linked HATP-based COFs—2D CCP-HATN, 2D CCP-BD, and 2D CCP-Th—were synthesized.[89,90] All of these frameworks exhibited an AA stacking model, with layer stabilization energies of −97, −113.1, and −117.4 kcal mol^{-1} for 2D CCP-HATN, 2D CCP-BD, and 2D CCP-Th, respectively (Fig. 8(b)–(d)). In addition, the larger BDAN and ThDAN molecules resulted

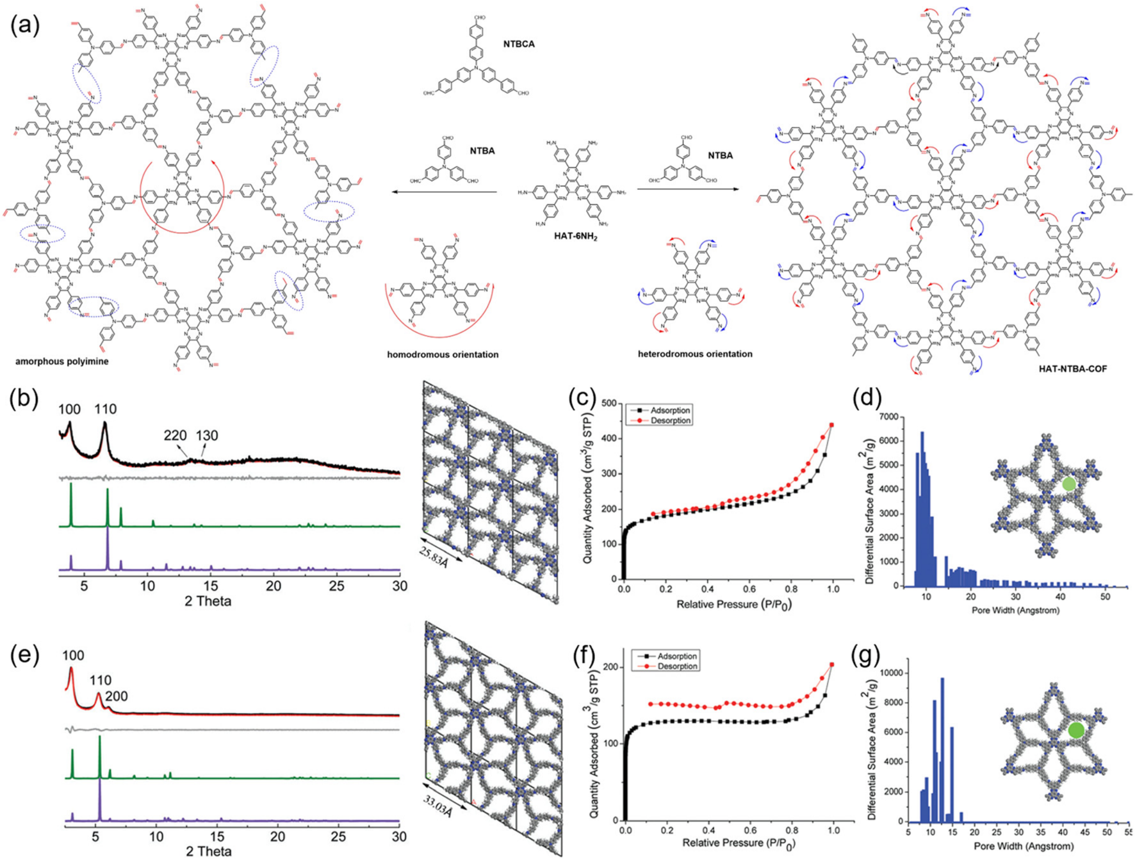

Fig. 7 (a) Construction of HATP-NTBA-COF using the variable orientation of imine linkages. (b) PXRD patterns of HATP-NTBA-COF. (c) N_2 adsorption–desorption isotherms of HATP-NTBA-COF. (d) Pore size distribution profiles of HATP-NTBA-COF. (e) PXRD patterns of HATP-NTBCA-COF. (f) N_2 adsorption–desorption isotherms of HATP-NTBCA-COF. (g) Pore size distribution profiles of HATP-NTBCA-COF. Reproduced with permission.[88] Copyright 2017, Royal Society of Chemistry.

in larger pore size distributions, specifically ranging from 1.0–1.3 nm and 1.8–2.0 nm (Fig. 8(e)–(g)). Comparative studies between imine-based HATN and olefin-based CCP-HATN revealed that the latter exhibited sharper and more well-defined redox bands, underscoring its superior redox activity as a cathode material in LIBs. Further investigation into its electronic and structural properties highlighted the role of thiophene incorporation in tuning charge transport characteristics. The bithiophene-based donor–acceptor framework (2D CCP-Th) possessed an extended conjugated skeleton. Ultraviolet-visible analysis indicated a reduced energy bandgap attributed to the efficient intramolecular charge transfer (ICT) between the electron-donating bithiophene unit and the electron-accepting HATN core. This charge delocalization substantially enhanced the electronic conductivity, which was crucial to achieve excellent rate performance as an electrode material.

The presence of additional cyano groups in olefin-linked HATP-based COFs, constructed *via* Knoevenagel polycondensation, induced significant structural twisting due to the steric hindrance effects. Therefore, the same group pioneered the first synthesis of unsubstituted olefin-linked HATP-based COFs—2D-PPQV1 and 2D-PPQV2—*via* the Horner–Wadsworth–Emmons reaction, utilizing Cs_2CO_3-mediated condensation of 1,4-bis(diethylphosphonomethyl)benzene and 4,4′-bis(diethylphosphonomethyl)biphenyl with HATN-6CHO in DMAc and mesitylene at 120 °C for 3 days, respectively.[94] PXRD patterns confirmed the formation of highly crystalline and dual-pore frameworks. These COFs exhibited exceptional thermal and chemical stability, combined with enhanced π-conjugation and a narrow bandgap, rendering them outstanding candidates for electrode materials with superior long-term cycling stability.

2.2.3 Dioxin-linked HATP-based COFs.

In dioxin-linked HATP-based COFs, ether bonds serve as a fundamental structural motif that significantly enhances chemical robustness, particularly under harsh environmental conditions.[95–97] These ether bonds were formed through an irreversible nucleophilic aromatic substitution reaction (SNAr), typically involving the reaction between halogen-functionalized HATP-based monomers (–F, –Cl, –Br) and hydroxyl compounds under base catalysis. The incorporation of these robust linkages endows the resulting dioxin-linked HATP-COFs with exceptional solvent resistance and high intrinsic electrical conductivity, making them potentially promising candidates for next-generation energy storage and conversion technologies.

Building on this, Xu *et al.* developed a high-yield, metal-free method for fabricating HOTT–HATN COF by combining

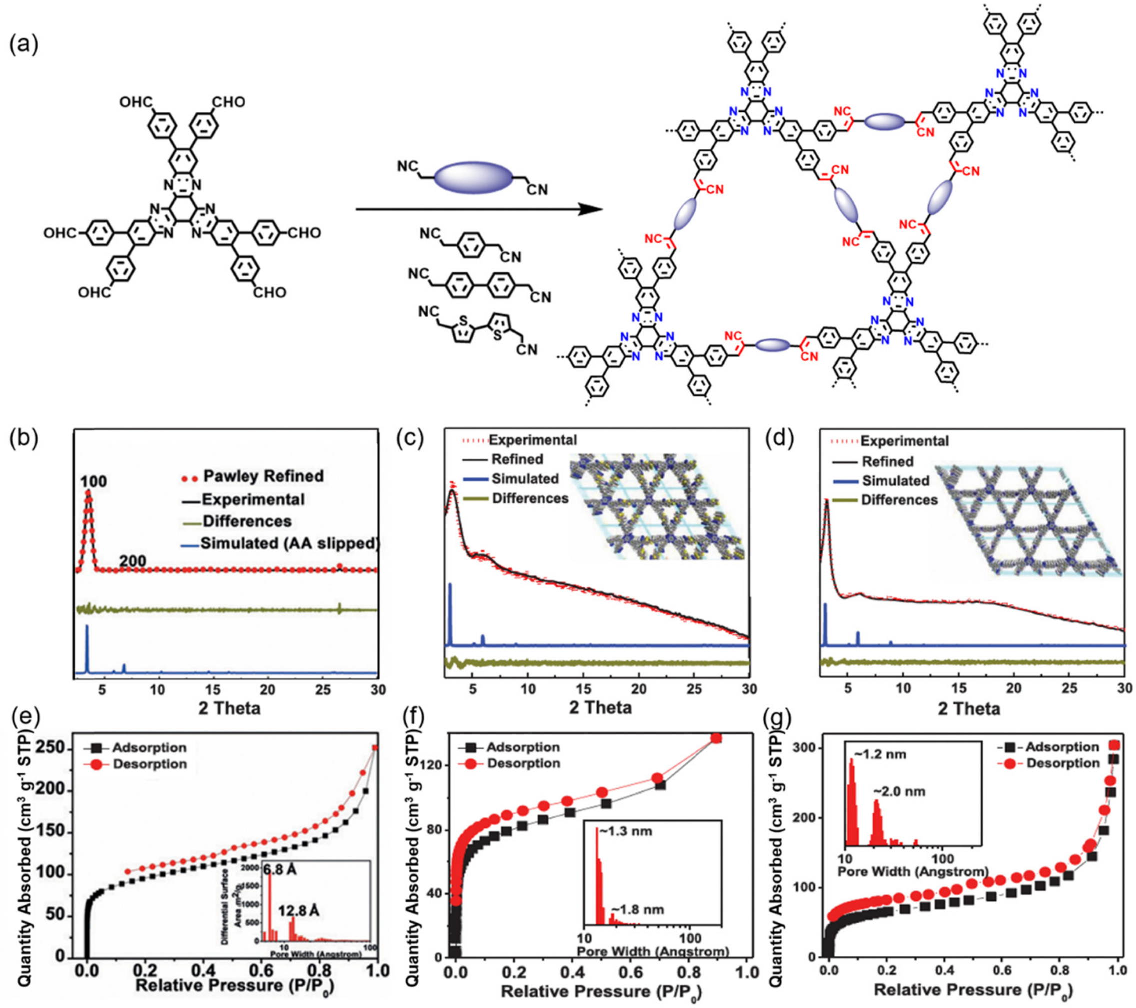

Fig. 8 (a) Synthetic route for the preparation of olefin-linked HATP-based COFs. (b) XRD patterns of 2D CCP-HATN. (c) XRD patterns of 2D CCP-Th. (d) XRD patterns of 2D CCP-BD. (e) N_2 adsorption–desorption isotherms and pore size distributions of 2D CCP-HATN. (f) N_2 adsorption–desorption isotherms and pore size distributions of 2D CCP-Th. (g) N_2 adsorption–desorption isotherms and pore size distributions of 2D CCP-BD. Reproduced with permission.[89] Copyright 2019, Wiley-VCH GmbH. Reproduced with permission.[90] Copyright 2021, Wiley-VCH GmbH.

2,3,6,7,10,11-hexahydroxytriphenylene (HOTT) and 2,3,8,9,14,15-hexachloro-5,6,11,12,17,18-hexaaza-trinaphthylene (HATN-Cl_6) as building blocks. The reaction was carried out in DMAc, with K_2CO_3 serving as the base catalyst at 170 °C for 5 days.[98] Additionally, the incorporation of both oxygen (O) and nitrogen (N) heteroatoms in the HOTT–HATN COF played a crucial role in establishing strong electron donor–acceptor (D–A) interactions, which significantly enhanced its redox properties.

Baek *et al.* made significant progress in constructing a highly crystalline HD-COF by refining the synthetic approach. They replaced HATN-Cl_6 with 2,3,8,9,14,15-hexafluoro-5,6,11,12,17,18-hexaazatrinaphthylene and optimized the reaction conditions using a K_2CO_3-mediated system in a mixed solvent of NMP and *o*-dichlorobenzene (*o*-DCB) at 180 °C for 3 days (Fig. 9(a)).[99] This adjustment led to enhanced crystallinity and improved charge transport properties. The PXRD analysis of HD-COF revealed well-defined diffraction peaks at 4.9, 8.6, 10.1, and 13.1°, corresponding to the (100), (110), (200), and (210) facets of the eclipsed 2D trigonal unit cell, respectively (Fig. 9(b)). Notably, the interlayer spacing (∼3.3 Å), attributed to π–π stacking interactions, facilitated efficient out-of-plane charge transport, a key factor for high-performance electrode materials. Further structural characterization through HR-TEM confirmed the presence of well-defined 1.7 nm micropore channels, consistent with fast Fourier transform (FFT) analysis results (Fig. 9(c) and (d)). Capitalizing on the superior structural properties of the bulk HD-COF material, they extended investigation to thin-film fabrication. A SiO_2 substrate was secured in a home-made Π-shaped polytetrafluoroethylene holder, which was placed in a Teflon-lined autoclave for solvothermal synthesis under standard conditions (Fig. 9(e)). Optical microscopy revealed uniform coloration and defect-free morphology at the macroscopic scale (Fig. 9(f)). AFM indicated HD-COF film thicknesses of 90–100 nm with a surface roughness below 10 nm, confirming smooth surface morphology (Fig. 9(g)). Additionally, grazing-incidence wide-angle X-ray scattering (GIWAXS) patterns (Fig. 9(h)) and *z*-axis line-cut profiles (Fig. 9(i)) validated the highly crystalline of HD-COF film. Combined its high electrical conductivity (1.58×10^{-1} S m^{-1})

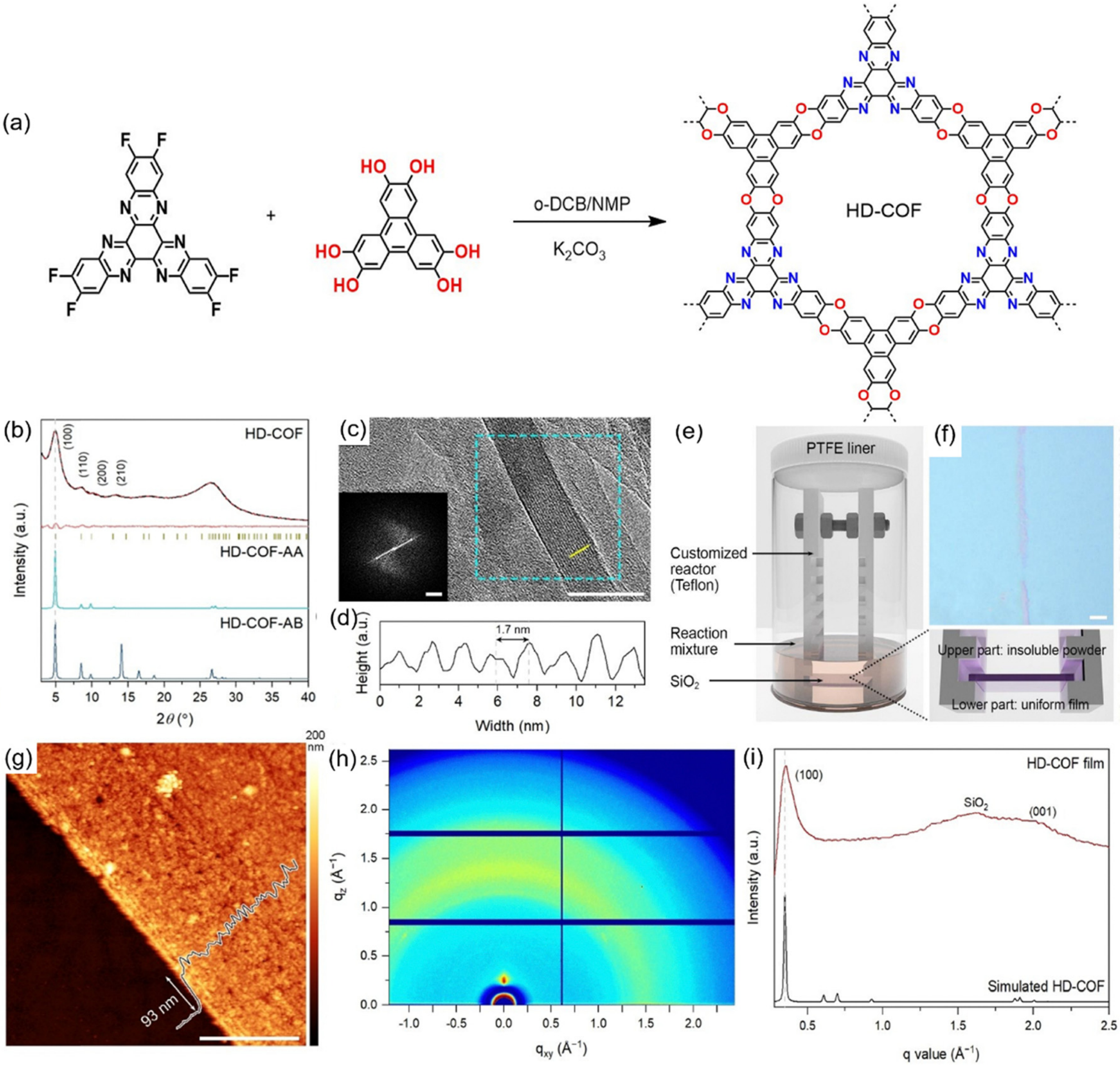

Fig. 9 (a) Synthetic route for the preparation of HD-COF. (b) PXRD patterns of HD-COF. (c) HR-TEM image of HD-COF. Inset: FFT of the image in the cyan square. (d) Line intensity profile of the lattice planes from the yellow line in (c), corresponding to the (010) plane of HD-COF. (e) Schematic illustration of the *in situ* fabrication of the HD-COF film. (f) Optical microscope image of the HD-COF film. Scale bar: 5 μm. (g) AFM image of HD-COF film. (h) GIWAXS of HD-COF film. (i) *z*-Axis linecut plot of HD-COF film.[99] Copyright 2023, Wiley-VCH GmbH.

and superior structural properties, HD-COF film showed promising potential for application as a binder-free electrode material in rechargeable batteries.

In a related development, Li *et al.* synthesized HATN-HHTP COF *via* an anhydrous Cs_2CO_3-catalyzed reaction in an NMP/mesitylene solvent system.[100] This approach capitalized on the structural benefits of its highly ordered porosity and extended conjugation, both critical for optimizing electronic conductivity and redox activity. The strategic integration of robust ether linkages, high conductivity, and tunable porosity in these COFs established their significant potential for high-performance energy storage applications.

2.2.4 Imide-linked HATP-based COFs.

Imide-linked HATP-based COFs represent an exciting and promising area of research that combines the structural advantages of COFs with the unique functionalities of imide linkages and HATP units, leading to enhanced chemical stability and redox activity. The most typical synthetic approach involved various amino and anhydride building blocks in the presence of solvents and catalysts (isoquinoline), which underwent an imidization to form polyimide structures.[101] The carbonyl functional groups in polyimides play a pivotal role, enabling reversible oxidation–reduction reactions, which make them highly suitable for use as high performance electrode materials through molecular design.[102]

A recent study by Huang *et al.* introduced a novel COF, HAHATN-PMDA-COF, synthesized through the condensation reaction between hexa(*p*-anilinyl) hexaazatrinaphthalene and pyromellitic dianhydride (PMDA) in a mixture of NMP, mesitylene and water with isoquinoline as a catalyst at 180 °C after 5 days (Fig. 10(a)).[103] The strong PXRD peaks observed at 3.52°, 7.03°, 9.31°, 10.56°, and 28.14° corresponded to (100), (200), (210), (300), and (001) facets, confirming the AA stacking mode (Fig. 10(b)). Additionally, HAHATN-PMDA-COF featured a 2D

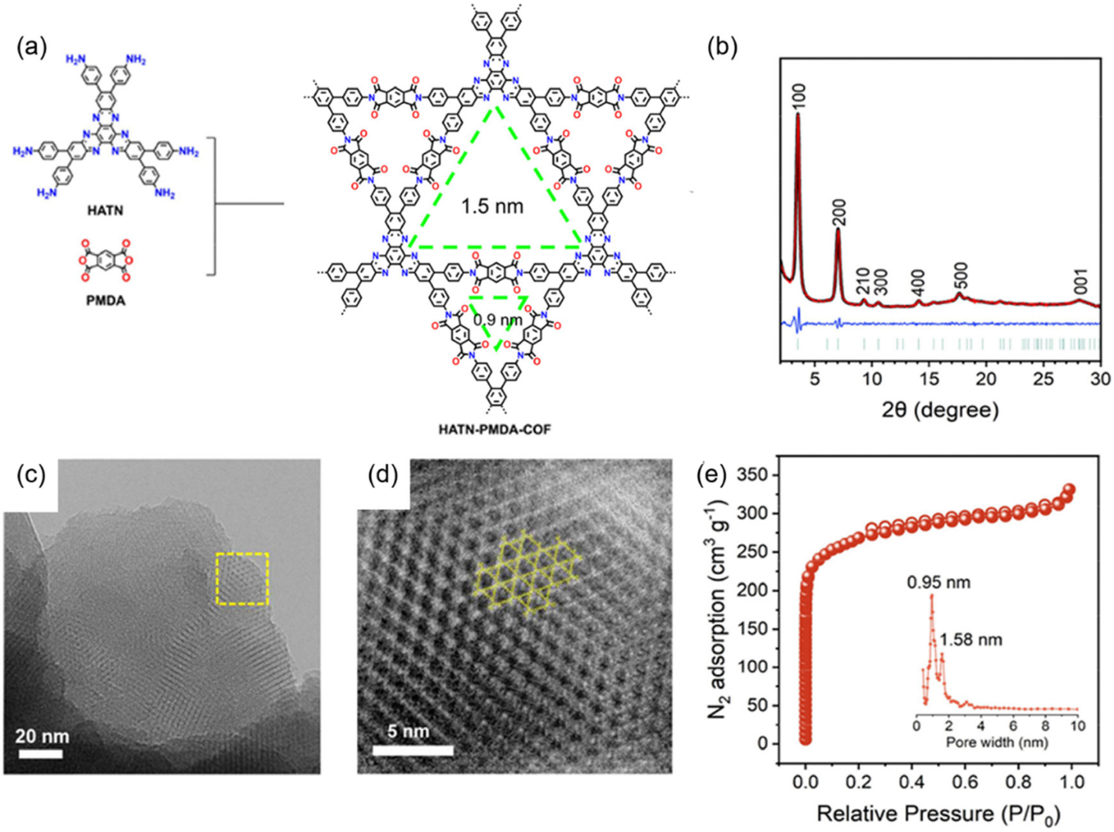

Fig. 10 (a) Synthetic route for the preparation of HAHATN-PMDA-COF. (b) PXRD patterns of HAHATN-PMDA-COF. (c) and (d) TEM images of HAHATN-PMDA-COF. (e) N_2 sorption isotherm profile (inset: pore size distribution) of HAHATN-PMDA-COF. Reproduced with permission.[103] Copyright 2024, Wiley-VCH GmbH.

trigonal structure with dual well-defined pores of 1.58 and 0.95 nm, which were the smallest pore sizes among the reported polyimide COFs (Fig. 10(c)–(e)). The high density lithophilic quinoxaline and phthalimide units within the uniform 1D channel of the COF make it a promising candidate for solid electrolyte interfacial in lithium metal anodes, facilitating the homogeneous deposition of Li^+ ions and suppressing the growth of lithium dendrites.

Jiang's group developed 2D HATN-AQ-COF by condensing 2,3,8,9,14,15-hexacarboxyl hexaazatrinaphthalene trianhydride (HATN-AP) with a redox-active linker, 2,6-diaminoanthraquinone (DAAQ), demonstrating a high theoretical capacity of 406 mA h g^{-1}.[104] The reaction was performed in the mixture of NMP, mesitylene and isoquinoline at 180 °C for 5 days. The PXRD patterns exhibited a sequence of diffraction peaks at 2.22°, 3.86°, 5.94° and 26.1°corresponding to (100), (101), (200), and (001) facets, respectively, which indicated a highly ordered and crystalline framework. The observed AA stacking mode was consistent with the pore size distribution of 3.8 nm calculated using density functional theory. HATN-AQ-COF exhibited an abundant pore structure and high specific surface area of up to 725 $m^2\ g^{-1}$, facilitating rapid ion transport (10^{-13} to 10^{-8} $cm^2\ s^{-1}$). These characteristics rendered it highly advantageous for use as a fast-charging electrode material.

The same group also developed redox-active 3D HATP-based COFs with cross-linked channels.[105] They synthesized two COFs, 3D-TP-HATN-COF and 3D-TAM-HATN-COF, which were synthesized from triphenylene-2,3,6,7,10,11-hexacarboxylic acid (HATNCA) and *N*,*N*,*N*′,*N*′-tetraphenyl-1,4-phenylenediamine and tetrakis(4-aminophenyl)methane, respectively (Fig. 11(a)). The diffraction peaks in PXRD patterns observed at 3.78, 4.89, 11.35, and 27.17° for 3D-TP-HATN-COF corresponded to the (211), (310), (716), and (12,9,1) facets, respectively (Fig. 11(b)). Similarly, 3D-TAM-HATN-COF exhibits distinct diffraction peaks at 4.24, 12.25, and 26.07°, which were indexed to the (211), (541), and (12,9,1) facets (Fig. 11(c)). Both materials showed high porosity with uniform pore sizes of 1.51 nm for 3D-TP-HATN-COF and 1.26 nm for 3D-TAM-HATN-COF, as well as interconnected 3D nanochannel networks (Fig. 11(d) and (e)). These structural features enable exceptional ion diffusion performance, achieving ion diffusion coefficients of 7.4×10^{-1} and 4.5×10^{-1} $cm^2\ s^{-1}$ for 3D-TP-HATN-COF and 3D-TAM HATN-COF, respectively. The strategy highlighted the critical role of ordered nanopores and tunable channel dimensions in optimizing ion transport kinetics, providing a robust platform for advanced high-energy density batteries.

2.2.5 Other groups-linked HATP-based COFs. Beyond the previously discussed linkers, phenylimino,[78] triazine,[79] and imidazole[106] have emerged as promising new linking units for HATP-based COFs. In particular, incorporating these functionalized linkers can significantly enhance the properties of

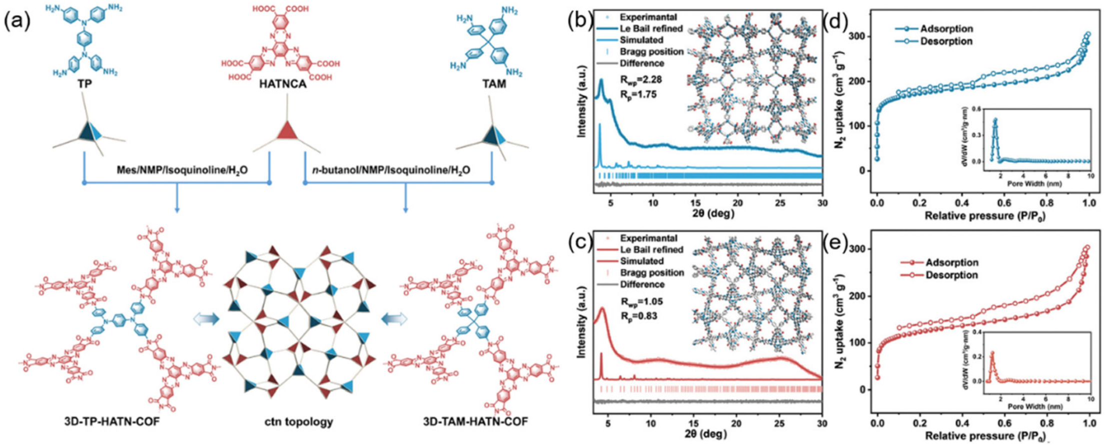

Fig. 11 (a) Synthetic route for the preparation of 3D-TP-HATN-COF and 3D-TAM-HATN-COF. (b) PXRD patterns of 3D-TP-HATN-COF. (c) PXRD patterns of 3D-TAM-HATN-COF. (d) N_2 adsorption–desorption isotherms of 3D-TP-HATN-COF. (e) N_2 adsorption–desorption isotherms of 3D-TAM-HATN-COF. Reproduced with permission.[105] Copyright 2025, Chinese Chemical Society.

HATP-based COFs, imparting unique electronic, chemical, and structural characteristics. This not only boosts the redox activity of the materials but also enables tunable porosity, improved chemical stability, and functional versatility, making them particularly suitable for energy storage applications.

For instance, the introduction of phenylimino into HATP-based COFs introduces intriguing redox-active properties. In a recent study by Lv *et al.*, a novel HPP-COF was synthesized in *N*,*N*-dimethylformamide by condensing BTA·4HCl and 1,4,5,8,9,11-hexaazatriphenylenehexacarbonitrile (HAT-CN) with Na_2CO_3 as a deacid reagent at 130 °C for 6 hours (Fig. 12(a)).[107] HPP-COF featured both pyrazine and phenylimino functional groups. Structural characterization by PXRD analyses revealed two broad peaks at 7.0° and 26.6°, corresponding to the (100) and (001) facets, respectively (Fig. 12(b)). The broad peak at 26.6° was attributed to the π–π stacking interactions between aromatic units in the framework, confirming a multi-layered structure of HPP-COF. HPP-COF retained its crystallinity even after 7 days of treatment with 6 M H_2SO_4 and 6 M NaOH as verified by the characteristic peaks in the PXRD patterns (Fig. 12(c)), which was advantageous as an electrode material in aqueous acidic and alkaline batteries.

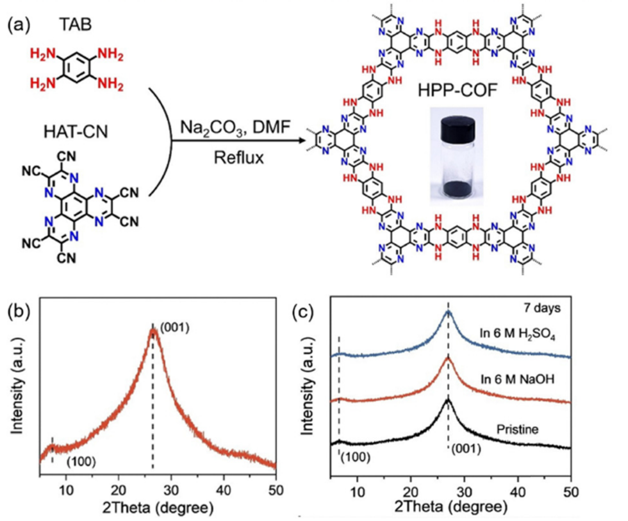

Fig. 12 (a) Synthetic route for the preparation of HPP-COF. (b) PXRD pattern of HPP-COF. (c) PXRD patterns of HPP-COF after treatments under 6 M NaOH and H_2SO_4 for 7 days. Reproduced with permission.[107] Copyright 2023, Wiley-VCH GmbH.

Building on their previous work with HPP-COF, Lv *et al.* also synthesized a novel COF, PTHATP-COF, by replacing BTA·4HCl with 2,3,5,6-tetraamine trihydrochloride in the design of PTHATP-COF, following the same approach.[108] PTHATP-COF exhibited excellent crystallinity, further demonstrating that the regulation of amino building blocks could lead to high crystallinity while allowing for the introduction of functionalized groups. Featuring pyrazine and phenylimino units, PTHATP-COF showed remarkable performance as an electrode material in calcium-ion batteries, highlighting its potential for tuning the properties of these COFs for diverse applications.

Strategic incorporation of C=O groups into phenylimino-linked HATP-based COFs (HTCOF) was pioneered by Yan *et al.* to amplify aromaticity and promote long-range electron delocalization.[109] This innovative design was realized through the condensation of TABQ and HAT-CN. HTCOF exhibited extended π-conjugation with fully delocalized electronic states and optimized band structures, achieving an intrinsic electrical conductivity of 3.9×10^{-1} S m^{-1}. Such exceptional charge transport properties enhanced redox activity and electron affinity, which enabled ultrafast ion storage kinetics, positioning it as a promising electrode material for next-generation energy storage systems.

Triazine, a six-membered aromatic ring with electron-deficient characteristics, has been explored as a linkage in HATP-based COFs to enhance redox activity and stability. Voort *et al.* synthesized HATN-CTFs by using diquinoxalino[2,3-*a*:2′,3′-*c*]phenazine-2,8,14-tricarbonitrile (HATN-3CN) as the starting material and $ZnCl_2$ as a molten salt at 400 °C for 48 h.[110] Two distinct covalent triazine frameworks were obtained by varying the $ZnCl_2$/monomer ratio, specifically, 5 : 1 and 10 : 1, which controlled the final structural characteristics. The higher $ZnCl_2$ concentration led to the formation of HATN-CTF-2, which exhibited a larger BET surface area and improved pore volume, suggesting better charge transport in energy storage devices. The research group further extended their work by post-synthetically metalating the HATN framework with copper(II) acetate, which significantly enhanced its catalytic activity, particularly in the Henry reaction of aromatic aldehydes and nitromethane under mild conditions.[111]

Additionally, imidazole, a heterocyclic aromatic compound with two nitrogen atoms in its five-membered ring, has proven to be an ideal linking unit in COFs.[112] Its coordination ability to cations and redox-active properties make it particularly suitable for use in energy storage applications. El-Kaderi *et al.* synthesized imidazole-linked HATP-based COFs, known as BCOF-1, by condensing HAHATN and TA, adopting a solvothermal synthesis in 1,4-dioxane and mesitylene with acetic acid catalysis at 120 °C for 5 days (Fig. 13).[106] The PXRD pattern of BCOF-1 closely matched the simulated diffraction pattern of an eclipsed AA model, confirming its well-ordered crystallinity. The honeycomb-like structure observed in the HR-TEM images was a hallmark of 2D materials. This ordered porous architecture and π-conjugated structure synergistically facilitated rapid ion diffusion coefficient (1.09×10^{-12} cm^2 s^{-1}) and substantial electronic conductivity (5.13×10^{-3} S m^{-1}), demonstrating its great potential as a high-performance electrode material.

Although the synthesis methods for HATP-based COFs mentioned above represent significant progress in terms of mild reaction conditions and simplicity, challenges remain in further expanding the diversity of linkage and topologies. Addressing these challenges will enable the development of designable and functional materials with tailored properties, broadening their applicability across various fields. This progress holds great promise for advancing future research and applications in energy storage.

3. Applications of HATP-based COFs in rechargeable batteries

The unique chemical structures of HATP-based COFs endow them with superior electrochemical performance. Their electronegative skeletons are situated within well-defined 1D channels, which are ideally suited for accommodating and rapidly transporting metal cations (Li^+, Na^+, K^+, and Zn^{2+}). The delocalized electrons within the fused extended π-system significantly enhance the framework's conductivity and stability, which is critical for achieving fast charge efficiency and long cycling stability in rechargeable batteries.[113] During the discharge process, the n-type C=N bonds of these materials undergo reduction, causing cleavage of the π bond and the formation of negatively charged nitrogen atoms due to their higher electronegativity.[114] Simultaneously, Li^+ are intercalated and transported through the cathode, balancing the negative charge. In the reverse charging process, Li^+ are released back into the electrolyte, and the electrode materials undergo oxidation, restoring the neutral states of the C=N groups. This reversible mechanism allows these HATP-based electrodes to perform efficiently across multiple cycles.

In 2017, Loh's team made a significant advance, synthesizing π-conjugated HATN through a simple condensation process, paving the way further exploration of their Li storage

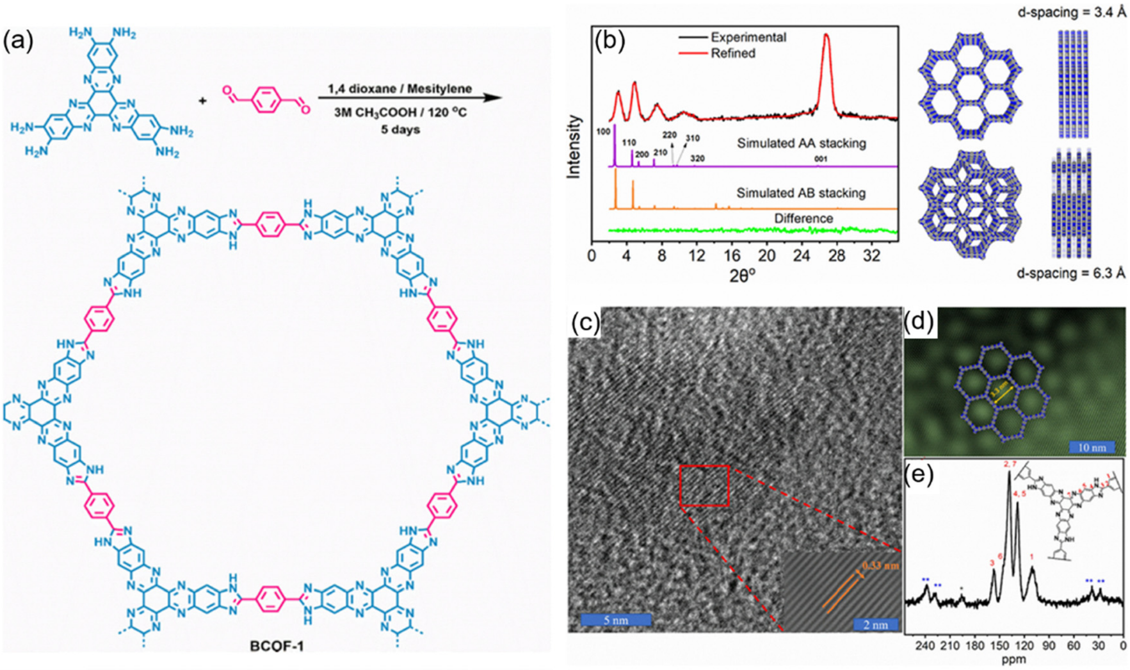

Fig. 13 (a) Synthetic route for the preparation of BCOF-1. (b) PXRD patterns of BCOF-1. (c) and (d) TEM images of BCOF-1. (e) Solid-state NMR of BCOF-1. Reproduced with permission.[106] Copyright 2024, American Chemical Society.

mechanisms.[113] A key aspect of their work involved the use of ^{15}N solid-state nuclear magnetic resonance (NMR) to probe the different lithiation states of the HATN. In the discharged state, the NMR spectra revealed the N1 peak disappeared, and the appearance of new peaks (N2, N3, N4), indicating that the HATN molecule coordinated with one Li^+ (forming 3Q-Li). With further discharge to 1.12 V, the final lithiated state (3Q-6Li) was confirmed by the increased intensity of the N5 resonance at −302 ppm. The DFT simulation revealed two discharge plateaus in the voltage range of 2.6–2.15 V (stage 1) and 1.68–1.38 V (stage 2). These results demonstrated that the HATN compound underwent a two-step lithiation process, with each step involving the transfer of three electrons, resulting in a high theoretical capacity of 418 mA h g^{-1}. This work laid the foundation for the design and optimization of HATP-based cathodes which had the potential to surpass traditional inorganic cathodes in specific capacity and energy density.

HATP-based COFs show great promise for various energy storage applications, especially as electrode materials in rechargeable batteries. Their high-dense redox-active sites, electronegative channels, π-conjugated structure, excellent stability, and tunable electronic properties make them ideal candidates for use in LIBs, SIBs, PIBs as well as AZIBs. The modular and tunable nature of HATP-based COFs allows for precise control over their structural properties. Ongoing research aimed at enhancing performance and optimizing synthesis methods will undoubtedly unlock the full potential of HATP-based COFs in next-generation energy storage devices.

3.1 HATP-based COFs electrodes for LIBs

The application of HATP-based COFs as electrode materials for LIBs began to gain attention in 2019. Table 1 summarizes the overall electrochemical performance of various HATP-based COFs. To achieve HATP-based COFs electrodes with excellent electrochemical performance, particularly in terms of reversible capacity, extended cycle stability, and superior rate capability, advanced synthetic methodologies and modification strategies have been systematically proposed. These include the incorporation of a conductive carbon matrix (morphology optimization and conductivity enhancement) and rational chemical structure engineering.

Electrochemical Li-storage properties of the HATP-based COFs were evaluated using CR2032-type coin cells assembled in argon-filled glove box (the oxygen and water concentration maintained below 1 ppm). The working electrode was fabricated by mixing redox-active materials (HATP-based COFs), conductive carbon and binder at an optimized ratio in NMP to form a slurry, which was subsequently casted on the current collector and dried under vacuum. Li foil was used as the counter electrode, while the electrolyte was selected based on the operating voltage windows (1 M lithium bis((trifluoromethyl)sulfonyl)azanide (LiTFSI) in 1,3-dioxane (DOL) and dimethoxyethane (DME) (1 : 1, v/v) for cathode and 1 M lithium hexafluorophosphate ($LiPF_6$) in ethylene carbonate (EC) : diethyl carbonate (DEC) (1 : 1, v/v) for anode).[124] A Celgard polyethylene porous membrane was utilized as the separator.

3.1.1 Incorporation of conductive carbon matrix. The initial research conducted by Feng *et al.* on the olefin-linked 2D CCP-HATN as a cathode material for LIBs revealed important insights into its electrochemical performance and limitations (Fig. 14).[89] The study showed that the pure 2D CCP-HATN cathode had a relatively low capacity of 62.5 mA h g^{-1} at 0.1 A g^{-1}, which was far below its theoretical value of 117 mA h g^{-1} and corresponded to a mere 53% utilization of the redox-active sites. This inefficiency was attributed to two main factors. First, the strong π–π interactions between adjacent layers caused the redox-active sites to be deeply embedded, limiting the electrolyte's access to these sites. In addition, the intrinsic electrical conductivity of the 2D CCP-HATN was very low (9.1×10^{-10} S cm^{-1}), restricting electron transport.

To address these challenges, the team explored a novel approach by *in situ* growing 2D CCP-HATN on the surface of carbon nanotubes (CNTs) during a solvothermal reaction, resulting in the formation of the 2D CCP-HATN@CNT hybrid material. This hybrid was intended to improve both the exposure of redox-active sites and the electrical conductivity. PXRD and SEM results indicated that when the amount of CNTs was optimized to 50%, the 2D CCP-HATN could be uniformly coated onto the CNTs. This optimization of morphology and structure led to a significant enhancement of the hybrid material's electrical conductivity (4×10^{-1} S cm^{-1}), which in turn improved the rate capability (94 mA h g^{-1} at 1 A g^{-1}). As a result, the electrochemical performance of the 2D CCP-HATN@CNT was significantly better than that of the pure 2D CCP-HATN. 2D CCP-HATN@CNT showed a stable capacity (116 mA h g^{-1} at 0.1 A g^{-1}), reflecting 73% utilization of redox-active sites after accounting for the contribution from the CNTs. In addition, the hybrid material also retained 91% of its initial capacity after 1000 cycles at a current rate of 0.5 A g^{-1}, demonstrating stable performance under fast charging/discharging conditions. This approach effectively addressed the issues of low electronic conductivity, slow Li^+ diffusion and buried redox-active sites, significantly improving COF-based electrode performance. However, the presence of large non-redox portions in the 2D CCP-HATN structure still limited both the theoretical and practical capacity.

To further enhance specific capacity, it was crucial to reduce the proportion of redox-inactive sites, or introduce external redox-active sites in the frameworks. Li *et al. in situ* incorporated CNTs onto the outer surface of HATN–HHTP to regulate morphology, giving rise to a core–shell structure (HATN–HHTP@CNT).[100] The electrical conductivity of the HATN–HHTP@CNT was enhanced (0.05 S cm^{-1}) to seven orders of magnitude higher than that of HATN–HHTP (4.8×10^{-9} S cm^{-1}). The discharge capacity was 230 mA h g^{-1} for the HATN–HHTP@CNT, closely approaching the theoretical capacity for a six-electron transfer mechanism and indicating a nearly ideal electrochemical performance. Remarkably, it still retained 100% capacity after 6900 cycles, a duration of over 4100 hours cycling, which was attributed to the stable chemical bond, π–π interaction, and pseudocapacitive effect.

Liu *et al.* developed an imide-linked HATP-based COF (HCBHAT-PH) with high-density redox-active C=N and C=O groups and incorporated carboxyl-functionalized carbon

Table 1 HATP-based COFs electrodes for rechargeable batteries

Materials	Electronic conductivity (S m^{-1})	Metal-ion battery	Electrode type	Voltage range (V)	Capacity (mA h g^{-1}), current density (A g^{-1})	High-rate capacity (mA h g^{-1}), current density (A g^{-1})	Capacity retention (%), current density (A g^{-1}), cycles	Ref.
NTCDI-COF	1.7×10^{-6}	LIBs	Cathode	1.5–3.5	210, 0.1	157, 5	86%, 2, 1500	67
PGF-1	3×10^{-3}	LIBs	Cathode	1–3.6	842, 0.1	189, 5	78.3%, 0.5, 1400	83
USTB-6@G	Not mentioned	LIBs	Cathode	1.2–3.9	285, 0.0544	188, 2.72	70%, 6000, 1.36	76
CCP-HATN@CNT	40	LIBs	Cathode	1.2–3.9	116, 0.1	94, 1	91%, 0.5, 1000	89
HATN-HHTP@CNT	5	LIBs	Cathode	1.2–3.8	230, 0.05	130, 2	100%, 0.5, 6900	100
HATN-AQ-COF	2.2×10^{-2}	LIBs	Cathode	1.2–3.9	319, 0.179	226, 3.58	80%, 3.58, 3000	104
HAPT-COF@rGO	Not mentioned	LIBs	Cathode	1.2–3.6	558, 0.0788	318, 7.88	92%, 7.88, 1000	115
BQ1-COF	3.1×10^{-6}	LIBs	Cathode	1.2–3.5	502.4, 0.0385	170.7, 7.73	81%, 1.54, 1000	116
cHATN-CTF	Not mentioned	LIBs	Cathode	1–4.5	310, 0.1	77, 2	Not mentioned	117
aHATN-CTF	Not mentioned	LIBs	Cathode	1–4.5	64, 0.1	10, 2	Not mentioned	117
aHATN-CTF	Not mentioned	LIBs	Anode	0.01–3	1171, 0.1	320, 10	82.9%, 1, 2000	117
HATN-HHTP@CNT	5	SIBs	Cathode	1–3.4	225, 0.05	128, 2	100%, 1, 6200	100
3D-TP-HATN-COF	Not mentioned	SIBs	Cathode	1–4.1	250, 0.2	206, 10	93%, 10, 8000	105
3D-TAM-HATN-COF	Not mentioned	SIBs	Cathode	1–4.1	202, 0.2	164, 10	82%, 10, 8000	105
HTCOF	3.9×10^{-1}	SIBs	Cathode	2.8–3.9	157.1, 0.16	53.5, 10	94.8%, 10, 10 000	109
TQBQ-COF	1.973×10^{-7}	SIBs	Cathode	0.8–3.7	452, 0.02	134.3, 10	96.4%, 1, 1000	118
HATN-PD-COF	3.69×10^{-4}	SIBs	Cathode	1–3.6	210, 0.2	195, 10	91%, 10, 7000	119
HATN-TAB-COF	2.96×10^{-4}	SIBs	Cathode	1–3.6	150, 0.2	140, 10	100%, 10, 3000	119
BCOF-1	5.13×10^{-3}	SIBs	Anode	0.01–3	370, 0.0393	50, 5.895	77%, 1.179, 400	106
HATN-HHTP@CNT	5	KIBs	Cathode	1.2–3.8	218, 0.05	120, 0.5	86.5%, 0.5, 2400	100
CPT	1.58×10^{-1}	KIBs	Anode	0.05–3	351, 0.1	186, 2	87%, 0.1, 200	82
TQBQ-COF	3.45×10^{-6}	KIBs	Anode	0.01–3	423, 0.03	185, 3	90.9%, 0.9, 600	120
PA-COF	Not mentioned	AZIBs	Cathode	0.2–1.6	265, 0.05	68, 10	74%, 1, 10 000	68
HA-COF	Not mentioned	AZIBs	Cathode	0.2–1.6	164, 0.1	35.4, 10	75.3%, 5, 10 000	121
HAQ-COF	Not mentioned	AZIBs	Cathode	0.2–1.6	339, 0.1	95.6, 10	88%, 5, 10 000	121
D-HATN	Not mentioned	AZIBs	Cathode	0.1–1.3	166, 1	101, 20	42.2%, 5, 10 000	122
GDAQ	Not mentioned	AZIBs	Cathode	0.1–1.6	331, 0.1	207, 15	90%, 10, 20 000	123
GDA	Not mentioned	AZIBs	Cathode	0.1–1.6	255, 0.1	100, 10	80%, 10, 20 000	123

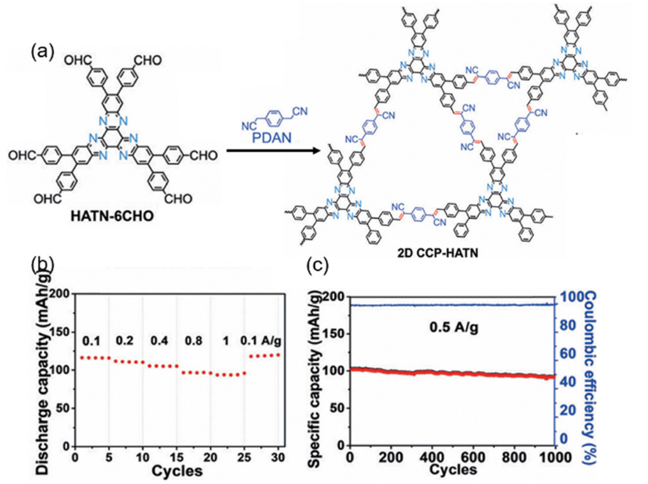

Fig. 14 (a) Synthetic route for the preparation of 2D CCP-HATN. (b) Rate performance of 2D CCP-HATN. (c) Cycling performance at 0.5 A g^{-1} of 2D CCP-HATN. Reproduced with permission.[89] Copyright 2019, Wiley-VCH GmbH.

nanotubes *in situ* into the COF structure.[125] This strategy achieved enhanced conductivity (1.18×10^{-1} S m^{-1}) and Li^+ diffusion kinetics (10^{-14} to 10^{-8} cm^2 s^{-1}), coupled with a uniform morphology of HCBHAT-PH on carboxyl-functionalized carbon nanotubes, resulting in high reversible capacity (303 mA h g^{-1} at 0.1 A g^{-1}) and 73% utilization of redox-active sites.

The subsequent introduction of conductive carbon materials, such as graphene and (rGO), to optimize the morphology and exfoliate stacked COFs into nanosheets has proven to be an extremely promising approach to enhance their electrochemical properties. Jiang *et al.* described the fabrication of conductive graphene during the synthesis of USTB-6 to fabricate a USTB-6@G composite, which was employed as a cathode material (Fig. 15(a)).[76] The HR-TEM analysis of USTB-6@G revealed lattice stripes similar to those of USTB-6, confirming that the USTB-6@G retained a crystalline structure after being dispersed onto graphene (Fig. 15(b)–(e)). The USTB-6 nanosheets had an average thickness of approximately 8.3 nm, which supported a high surface area, improving Li^+ diffusion during electrochemical reactions (Fig. 15(f)–(i)). These enhancements allowed the USTB-6@G composite to achieve a high capacity (285 mA h g^{-1} at 0.2C) (Fig. 15(j)), excellent rate performance (188 mA h g^{-1} at 10C) and superior stability (170 mA h g^{-1} at 5C after 6000 cycles) (Fig. 15(k)).

In a more recent study, HAPT-COF was synthesized through a one-step condensation method between CHHO and TAPT.[115] The resultant HAPT-COF exhibited a 2D π-conjugated, robust framework with abundant C=O and C=N functional groups, providing an ultrahigh theoretical capacity of 788 mA h g^{-1}. In the subsequent step, a post-hydrothermal reaction was employed between HAPT-COF and graphene oxide (GO), resulting in the formation of HAPT-COF@rGO, where GO was reduced to rGO (Fig. 16(a)). The efficient intercalation of HAPT-COF with rGO ensured that HAPT-COF were uniformly distributed and well-dispersed on rGO, forming a sheet morphology of HAPT-COF@rGO, which led to the exposure of redox-active centers, and enhanced electron transport and Li^+ diffusion (Fig. 16(b)–(i)). The strong π–π interactions between HAPT-COF and rGO not only improved conductivity but also helped maintain structural integrity. Theoretical simulations and practical characterizations revealed that up to 18 Li^+ could be stored reversibly per repeating unit of the framework in three distinct steps, thus achieving a substantial capacity (558 mA h g^{-1} at 0.1C) (Fig. 16(j)). In addition, the HAPT-COF@rGO composite cathodes also demonstrated excellent rate capability (318 mA h g^{-1} at 10C), along with 92% capacity retention after 1000 cycles (Fig. 16(k)). These *in situ* polymerization and exfoliation-related investigations provided feasible strategies for the effective utilization of the redox-active sites of COFs, as well as an improvement in conductivity, thus facilitating application as electrode materials.

3.1.2 Chemical structure engineering.

The addition of conductive carbon materials to COFs electrode materials for LIBs indeed contributed significant advantages in terms of improving overall electrochemical performance, including enhanced electrical conductivity, structural stability, Li^+ transport and fully exposed redox-active sites. However, these improvements come with trade-offs, particularly in terms of energy density. To mitigate this, it is essential to design and synthesize HATP-based COFs with adequate conductivity, multiple redox-active sites with optimized utilization, through reasonable molecular design. Optimizing these features can lead to excellent battery performance without requiring large amounts of carbon additives.

Chen *et al.* made significant advancements in developing a novel redox-active COF cathode material, BQ1-COF, which was synthesized *via* a direct condensation reaction between TABQ and CHHO (Fig. 17(a)).[116] The unique structure incorporated C=O groups with minimal redox-inactive groups, resulting in an exceptionally high reversible capacity (502.4 mA h g^{-1} at 39 mA g^{-1}), among the highest specific capacities ever reported for LIBs (Fig. 17(b)). However, BQ1-COF exhibited a capacity retention of 81% at 1.54 A g^{-1} after 1000 cycles with fluctuating Coulombic efficiency (Fig. 17(c)). The electrochemical behavior of BQ1-COF was governed by the reversible reaction of Li^+ with the C=O and C=N groups in the framework. During the discharge process, up to 12 Li^+ participated reversibly in the redox reaction in four distinct steps (Fig. 17(d)). The reaction involved the reduction of the carbonyl (C=O) and imine (C=N) groups, followed by re-oxidization during the subsequent charge process. However, the stability of the lithiated structure tended to decrease as more Li^+ became involved in the redox process. The upper limitation appeared to be 12 Li^+, beyond which the structural integrity and electrochemical performance might deteriorate.

Moreover, Jiang *et al.* enhanced the stability and electrochemical performance of HATP-based COFs by constructing a redox-active imide-based structure, resulting in the development of HATN-AQ-COF. This material, with fully conjugated nature, well-defined porous network and densely redox-active sites, synergistically demonstrated exceptional charge transfer characteristics, achieving rapid ion diffusion coefficient (10^{-13} to 10^{-8} cm^2 s^{-1}) and high electrical conductivity (2.2×10^{-4} S cm^{-1}), all of which contributed to its outstanding electrochemical properties

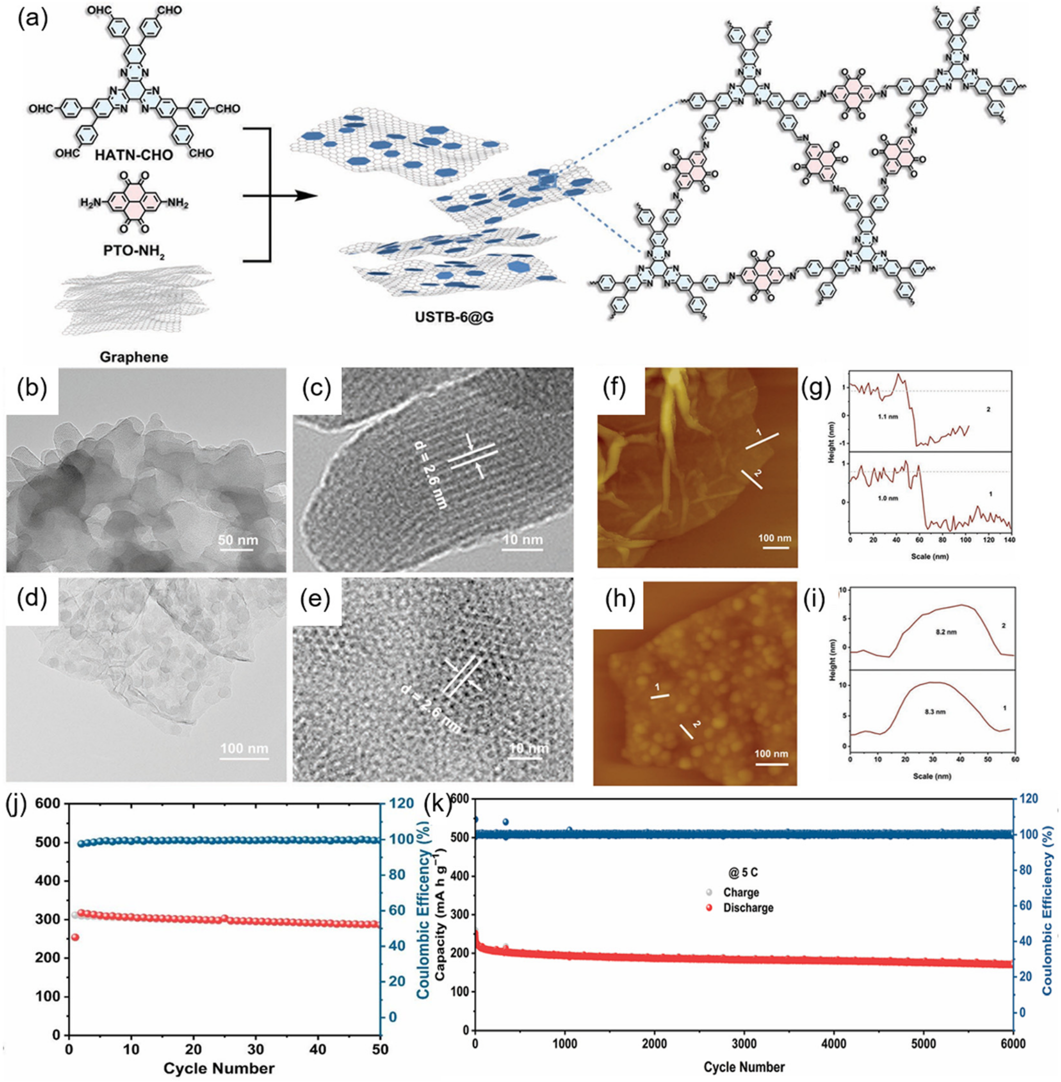

Fig. 15 (a) Synthetic route for the preparation of USTB-6@G. (b) and (c) TEM images of USTB-6@G. (d) and (e) TEM images of USTB-6. (f) and (g) AFM topography images and AFM height profiles of graphene. (h) and (i) AFM topography images and AFM height profiles of USTB-6@G. (j) Cycling performance of USTB-6@G at 0.2C. (k) Cycling performance of USTB-6@G at 5C. Reproduced with permission.[76] Copyright 2022, Wiley-VCH GmbH.

(Fig. 18).[104] As a result, HATN-AQ-COF achieved a high capacity (319 mA h g^{-1} at 0.5C). Even at a high-rate of 10C, it retained 80% of its initial capacity after 3000 cycles, demonstrating exceptional cycling stability and rate performance.

To elucidate the underlying charge storage mechanism, an analysis of Li^+ absorption energies was conducted, revealing a sequential multi-site coordination process. Initially, Li^+ preferentially binds to the C═N groups in the HATN units (site A), followed by interactions with the C═O groups in quinone moieties (site B). Subsequently, Li^+ coordinates with the C═N groups in the HATN units (site A) and the C═O groups in imide moieties (site C), enabling an overall 12-electron transfer process (Fig. 18(d) and (e)). This study underscores the importance of integrating multiple redox-active sites to enhance the utilization of existing redox-active sites. By strategically tailoring the spatial distribution and electronic environment of these sites within the framework, researchers can further enhance energy storage capacity, rate capability, and long-term cycling stability. Such structural refinements pave the way for the development of next-generation COF-based electrode materials with superior electrochemical performance, catering to the growing demands of high-performance energy storage technologies.

Because of their electronegative nature, HATP-based COFs predominantly function as cathode materials, where n-type C═N groups facilitate reduction reactions during discharge (Li^+ insertion) and oxidation reactions during charge (Li^+ extraction). However, recent studies have shown that under certain conditions, these materials can also exhibit bipolar behavior, enabling them to operate at higher voltages and achieve greater energy density.

Zhu *et al.* investigated the impact of $ZnCl_2$ concentration and reaction time on the crystallinity of the resulting HATN-CTF, which was developed by building on the ionothermal trimerization of HATN-3CN.[117] When $ZnCl_2$ was used in lesser

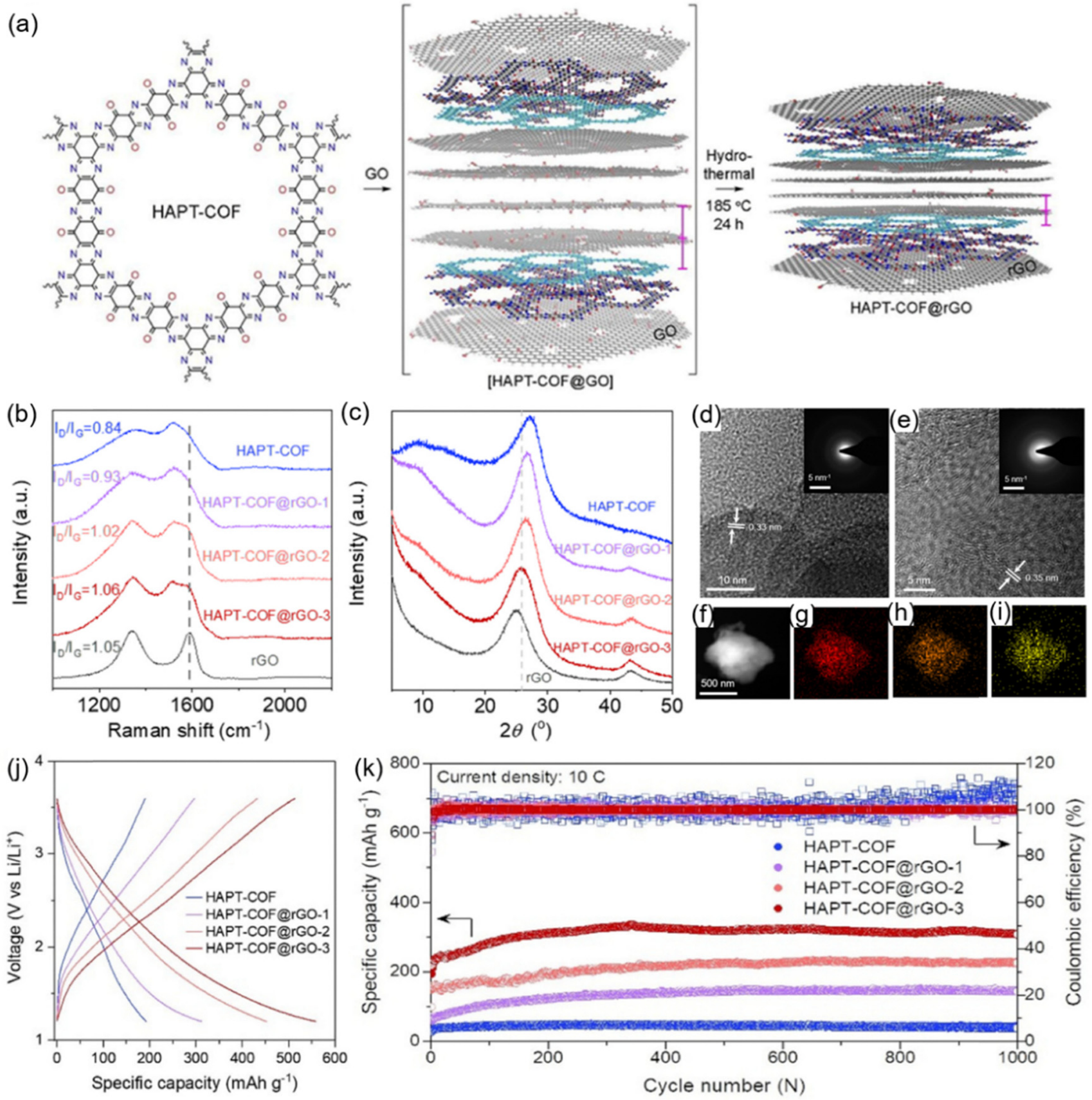

Fig. 16 (a) Synthetic route for the preparation of HAPT-COF@rGO. (b) Raman spectra and PXRD patterns of HAPT-COF and HAPT-COF@rGO. (c) TEM images of HAPT-COF. (d) HR-TEM images of HAPT-COF. (e) HR-TEM images of HAPT-COF@rGO. (f)–(i) The corresponding mapping images of C, N and O elements for HAPT-COF@rGO. (j) The galvanostatic charge/discharge curves at 0.05C. (k) Cycling performance at 10C. Reproduced with permission.[115] Copyright 2024, Elsevier.

amounts and the reaction time was short, the resulting cHATN-CTF exhibited a crystalline structure, which was consistent with the simulated eclipsed AA stacking model. However, due to its low specific surface area of 41.52 $m^2\ g^{-1}$ and strong π–π interactions, cHATN-CTF provided limited accessible redox-active sites for Li^+ interaction, resulting in a relatively low discharge capacity of 70 mA h g^{-1} within a voltage range of 1.0–4.5 V. In contrast, increasing $ZnCl_2$ concentration and extending the reaction time, (monomer/$ZnCl_2$ of 1 : 10 and a reaction time of 48 hours), yielded an aHATN-CTF with higher surface area and a porous structure. These effects, significantly improved the ability of aHATN-CTF to store and release cations, leading to a substantial capacity (251 mA h g^{-1} at 50 mA g^{-1}). Notably, unlike other HATP-based COFs, the presence of electron-deficient triazine rings at higher voltages enabled HATN-CTF to bind with PF_6^- ions, further supporting its bipolar characteristics. This demonstrated that incorporating redox-active units with high potential, alongside precise polymerization control, could provide an effective strategy for tuning electrochemical properties, particularly in terms of capacity and operating voltage. Furthermore, the superlithiation of aHATN-CTF underscored its potential as an anode material. It achieved a high reversible capacity of 655 mA h g^{-1} at 1 A g^{-1} with an impressive capacity retention of 82.9% over 2000 cycles, positioning it as a promising candidate for next-generation organic anode materials.

3.2 HATP-based COFs electrodes for other alkali metal-ions batteries

SIBs and KIBs have emerged as a more sustainable alternative to LIBs due to the abundance and low cost of sodium and

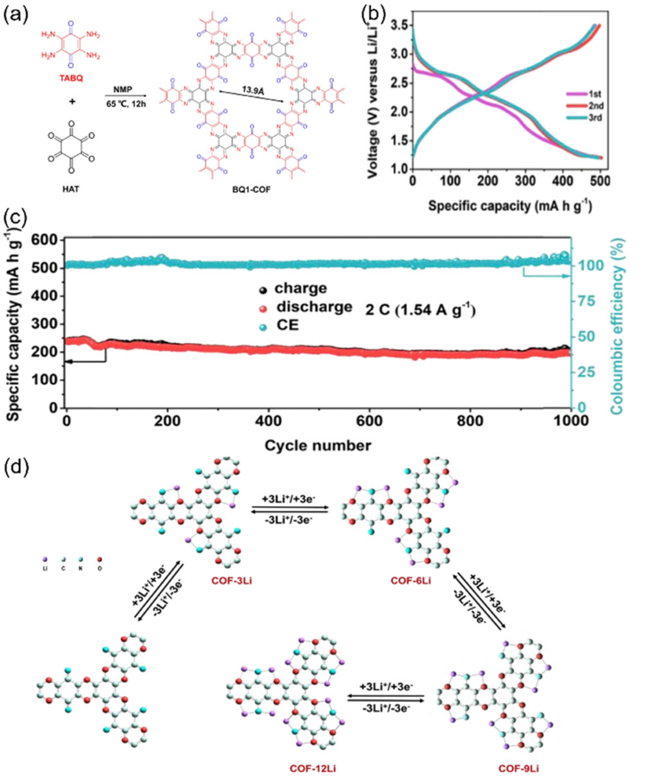

Fig. 17 (a) Synthetic route for the preparation of BQ1-COF. (b) The galvanostatic charge/discharge curves of BQ1-COF at 39 mA g^{-1}. (c) Cycling performance of BQ1-COF at 1.54 A g^{-1}. (d) Structure evolution during the discharge procedure of BQ1-COF. Reproduced with permission.[116] Copyright 2020, Elsevier.

potassium.[126–128] The standard potential (*vs.* standard hydrogen electrode) of K^+/K and Na^+/Na is −2.936 V and −2.714 V, respectively, giving PIBs a higher voltage and energy density compared to SIBs.[19] Given the current challenges of accommodating larger sized sodium-ions (Na^+) and potassium-ions (K^+) in traditional inorganic electrode materials, HATP-based COFs present a promising solution. The interconnected porous structures in COFs provide abundant ion transport channels, facilitating the rapid transport and accommodation of Na^+ and K^+.[62] Additionally, the designable structure of COFs enables the precise tuning of functionality in their building blocks, which enhances their metal-ion affinity (Na^+ and K^+), ultimately improving charge storage performance and stability.

Another key feature of HATP-based COFs is their high-density redox-active sites, specifically C═N groups within the HATP frameworks. These sites undergo reversible conversion reactions, particularly similar to those observed in LIBs during repetitive charge and discharge cycles. However, it is important to emphasize that the mechanisms for cation storage in SIBs and KIBs differ from those in LIBs. In PIBs, the π-electrons present in the aromatic rings of the COF structure can interact with K^+, creating additional binding sites that enhance cation storage and the overall capacity of the electrode materials. This unique synergy between structural and chemical features positions HATP-based COFs as transformative materials for advanced SIBs and KIBs, contributing significantly to the development of high-performance, sustainable energy storage materials.

The assembly processes of HATP-based COFs for SIBs and PIBs followed a similar protocol to LIBs, with the primary differences lying in the employment of separator and electrolyte. Typically, a Whatman glass microfiber filter was utilized as the separator, and the electrolyte systems were formulated using the corresponding alkali metal salts.[129]

3.2.1 Sodium-ion batteries.

Chen *et al.* were among the first to explore the application of HATP-based COFs in SIBs in 2020, demonstrating that TQBQ-COF also exhibited strong potential as a cathode material in LIBs.[118] The high-density nitrogen atoms within the TQBQ-COF framework played a crucial role to reduce the energy gap and enhance electronic conductivity (1.9×10^{-7} S m^{-1}), both of which were essential to achieve rapid charge/discharge kinetics and efficient charge transport. Notably, the ion storage mechanism of TQBQ-COF in SIBs differed significantly from that in LIBs. In the initial step, 6 Na^+ were coordinated to the N atoms in the HATP centers, followed by the coordination of an additional 6 Na^+ to adjacent nitrogen and oxygen atoms within the framework. The ability to accommodate up to 12 Na^+ contributed to the material's outstanding electrochemical performance, including a high reversible capacity (452 mA h g^{-1} at 0.02 A g^{-1}) within a voltage range of 1–3.6 V, excellent rate performance (134.3 mA h g^{-1} at 10 A g^{-1}), and remarkable cycling stability (96% capacity retained after 1000 cycles).

Building on the success of the HATP-based COFs in LIBs, Li *et al.* extended the application of *in situ* polymerization to SIBs, achieving remarkable electrochemical performance in HATN-HHTP@CNT composite cathodes through the incorporation of CNTs.[100] The *in situ* polymerization process facilitated the formation of a well-integrated conductive polymer network, which improved electronic conductivity and promoted the rapid Na^+ transport process during charge/discharge cycles. A particularly notable feature of HATN-HHTP@CNT in SIBs was its exceptional cycling stability, as it sustained 6200 charge/discharge cycles at 1 A g^{-1} with 100% capacity retention. This indicated the absence of significant capacity degradation over more than 1700 hours, marking a remarkable achievement for SIBs. The design strategy of HATP-based COFs with porous structures, high conductivity, and multiple redox-active sites remains a highly effective approach for enhancing SIBs performance.

While 2D COFs have demonstrated significant potential as cathode materials for SIBs, their intrinsic microporous structure presents a major challenge. With pore sizes typically below 2 nm, these materials impose considerable limitations on the diffusion of larger ions like Na^+, thereby restricting high-rate charge/discharge performance.

Jiang *et al.* synthesized two imide-linked HATP-based COFs containing a mesoporous structure—HATN-PD-COF and HATN-TAB-COF—*via* hydrothermal reactions using HATNCA with PDA and 1,3,5-tris(4-aminophenyl) benzene, respectively (Fig. 19(a)).[119] These COFs exhibited high crystallinity with an AA stacking configuration and featured mesopores of approximately 3.1 nm (HATN-PD-COF) and 2.0 nm (HATN-TAB-COF).

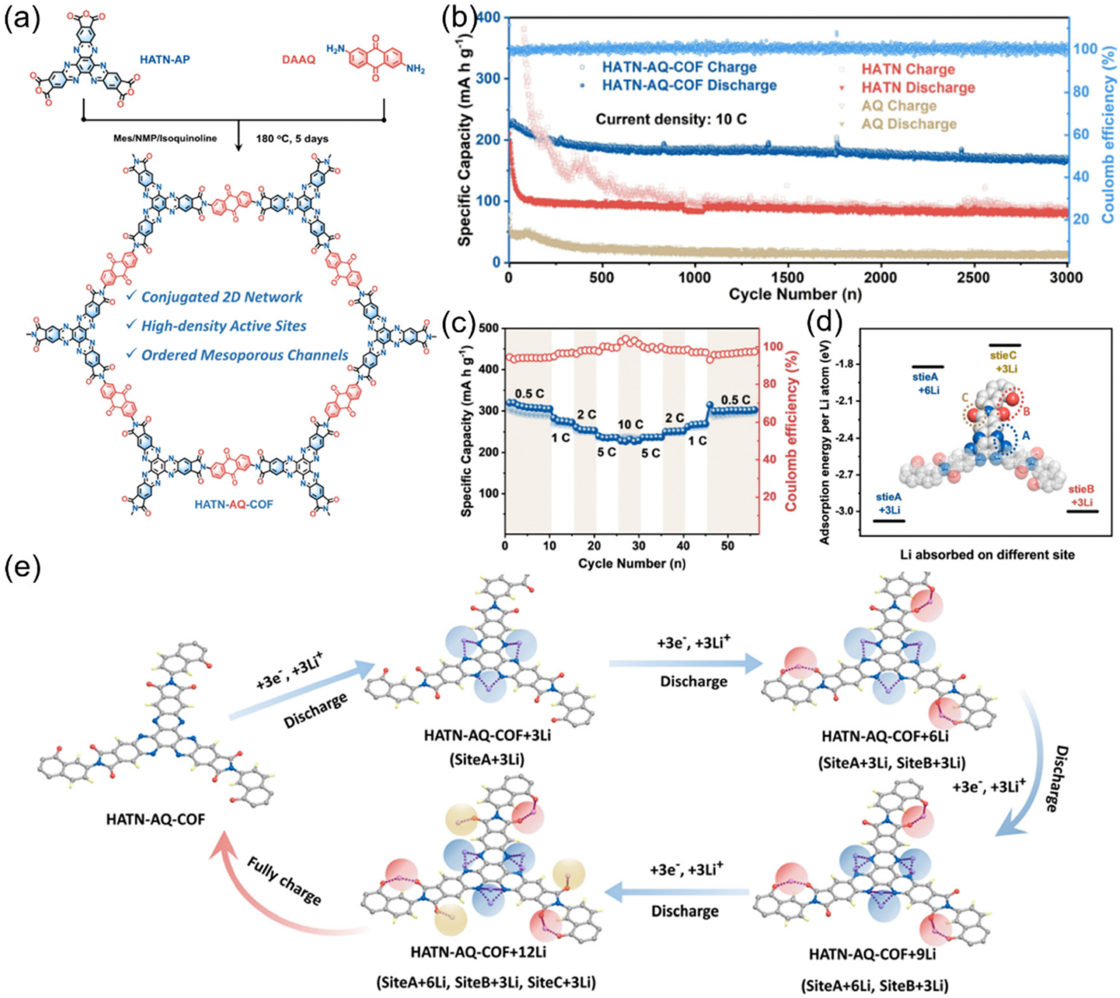

Fig. 18 (a) Synthetic route for the preparation of HATN-AQ-COF. (b) Cycling performance of HATN-AQ-COF at 10C. (c) Rate performance of HATN-AQ-COF. (d) Adsorption energy per Li^+ at different sites. (e) Structure revolution during the discharge procedure of HATN-AQ-COF. Reproduced with permission.[104] Copyright 2022, Wiley-VCH GmbH.

The larger pore size of HATN-PD-COF facilitated faster Na^+ transport, as evidenced by its higher diffusion coefficient of 10^{-9} cm^2 s^{-1} compared to the HATN-TAB-COF ($10^{-9.5}$ cm^2 s^{-1}). As a result, they demonstrated superior rate performance (195 mA h g^{-1} for HATN-PD-COF and 140 mA h g^{-1} for HATN-TAB-COF at 10 A g^{-1}), outperforming most reported organic cathodes (Fig. 19(b) and (c)). The higher capacity of HATN-PD-COF was primarily attributed to the denser distribution of redox-active sites within its structure. Moreover, the HATN-PD-COF cathode exhibited excellent capacity retention of 91% after extensive 7000 cycles at 10 A g^{-1} (Fig. 19(d)). The binding strength analysis suggested that the N atoms in the HATN unit (site I) provided a more energetically favorable environment for Na^+ coordination compared to the O atoms in the imide groups (site II) (Fig. 19(e)). Consequently, HATN-PD-COF achieved a more balanced and stable Na^+ storage process by initially occupying the stronger-binding site I, followed by the utilization of slightly weaker site II.

The same groups also developed 3D HATP-based COFs cathodes, 3D-TP-HATN-COF and 3D-TAM-HATN-COF, featuring cross-linked nanochannels and uniform pore sizes, which was also determined to be an effective strategy to enhance the ion transport in rechargeable batteries.[105] Benefiting from the rapid ion diffusion and co-storage of Na^+ and PF_6^-, the 3D-TP-HATN-COF cathode showed an ideal reversible capacity (250 mA h g^{-1} at 0.2 A g^{-1}), which was higher than that of 3D-TAM HATN-COF (202 mA h g^{-1} at 0.2 A g^{-1}), thanks to its high-density redox-active sites and larger channels. Additionally, the 3D-TP-HATN-COF cathode achieved an outstanding rate performance (206 mA h g^{-1} at 10 A g^{-1}) and high capacity retention of 93% after 8000 cycles at 10 A g^{-1}. Furthermore, the full battery, composed of 3D-TP-HATN-COF and Na_3Bi, exhibited the exceptional capacity of 195 mA h g^{-1} at 10 A g^{-1} after 1000 cycles.

HATP-based COFs demonstrated remarkable potential not only as cathodes but also anode applications for SIBs. Notably, El-Kaderi *et al.* investigated BCOF-1 as an anode material for Na^+ storage.[106] Apart from the inherent six redox-active sites in HATP units, the imidazole linkages generated during polymerization provided additional Na^+ coordination sites, significantly enhancing charge storage capacity. This synergistic combination

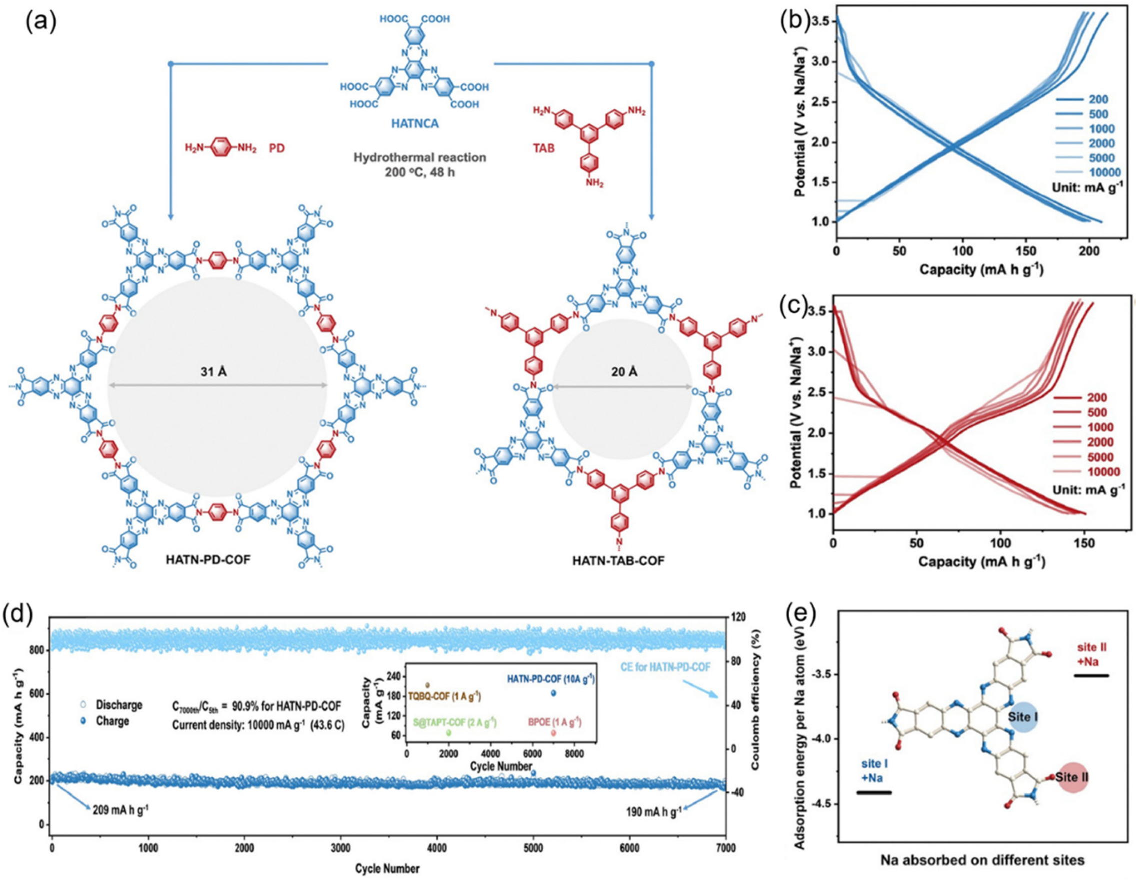

Fig. 19 (a) Synthetic route for the preparation of HATN-PD-COF and HATN-TAB-COF. (b) Rate performance of HATN-PD-COF. (c) Rate performance of HATN-TAB-COF. (d) Cycling performance of HATN-PD-COF at 10 A g^{-1}. (e) The adsorption energy per Na^+ at different sites of HATN-PD-COF. Reproduced with permission.[119] Copyright 2024, Springer.

of abundant redox-active sites, well-ordered pore structure, and extended π-conjugated frameworks contributed to a high reversible capacity (370 mA h g^{-1} at 0.1C), rate capability (50 mA h g^{-1} at 15C), and cycling stability (77% capacity retention after 400 cycles at 3C).

3.2.2 Potassium-ion batteries.

Among alkali metal-ions, K^+ exhibits unique properties, including a higher transfer number and greater mobility compared to other alkali metal-ions, primarily due to its weaker Lewis acidity. This results in rapid kinetics for PIBs. The strong interaction between cations and the π electrons of the aromatic rings has been identified as a crucial factor for π-conjugated 2D COFs for the storage of K^+, offering an additional pathway for enhancing electrochemical performance. Li *et al.* utilized the representative TQBQ-COF as the anode material for PIBs.[120] As in LIBs and SIBs, the C═O and C═N groups in TQBQ-COF serve as redox-active sites capable of reversibility with K^+. The distinguishing factor of PIBs compared to other alkali metal-ion batteries is the additional involvement of the C═C bonds in the framework. Fourier transform infrared (FT-IR) spectra revealed that the C═C groups of the TQBQ-COF reversibly disappeared and reappeared during the discharging and charging cycles, indicating that K^+ interacted directly with the π-electrons of the aromatic rings. This interaction enabled reversible modulation of the π-conjugation, providing additional capacity (423 mA h g^{-1} at 0.03 A g^{-1}) beyond the simple interaction towards K^+ with the C═O and C═N groups. Such a phenomenon has also been observed in multivalent ion batteries.[130] Guided by the π–cation interaction, this behavior highlights the versatility of π-conjugated materials in facilitating ion storage. The additional capacity arising from these interactions may be a key factor driving the success of π-conjugated HATP-based COFs in energy storage applications.

The HATN-HHTP@CNT composite, recognized for exceptional cycling stability in LIBs and SIBs, also demonstrated remarkable K^+ storage capabilities.[100] HATN-HHTP@CNT cathode delivered a high discharge capacity (218 mA h g^{-1} at 0.05 A g^{-1}) with characteristic voltage plateaus at 2.9–2.35 V and 2.0–1.5 V. These clear redox features revealed multi-step charge transfer processes, demonstrating a charge storage mechanism similar to that observed in LIBs and SIBs. Furthermore, the HATN-HHTP@CNT cathode exhibited ultralong cyclability with a capacity retention of 86.5% over 2400 cycles at 0.5 mA g^{-1}, highlighting its robust coordination and structural integrity.

3.3 HATP-based COFs electrodes for aqueous zinc-ion batteries

The low cost and high abundance of zinc has contributed to a growing interest in AZIBs, which offer a cost-effective and environmentally friendly alternative for large-scale energy storage applications.[131] Zinc is highly stable in aqueous electrolytes with a satisfactory theoretical specific capacity of 820 mA h g^{-1} and a suitable standard potential (*vs.* standard hydrogen electrode) of −0.76 V for Zn^{2+}/Zn.[132,133] Additionally, AZIBs combine high safety, cost-effectiveness, non-toxicity, and higher ionic conductivity, making them promising alternatives to conventional LIBs.

The use of HATP-based COFs as electrode materials for AZIBs represents an emerging area of research with great potential. A notable advantage of HATP-based COFs is their poor solubility in aqueous electrolytes, which contributes to structural robustness and exceptional long-term cycling stability. Certain HATP-based COFs exhibit the ability to cycle up to ten thousand cycles or more without significant degradation.

Determining the charge storage mechanism of organic electrode materials is a crucial factor in the context of AZIBs. The mechanism is primarily governed by the coordination interactions between active functional groups in the electrode material and the cations in the electrolyte. A key factor in this process is the competition between different cations, notably H^+ and Zn^{2+}, which significantly impacts both capacity and rate performance.

For the fabrication of AZIBs, the electrode slurry—containing HATP-based COF, conductive additive and binder—was typically coated onto stainless steel or carbon paper current collectors. The electrochemical system employed $ZnSO_4$ electrolyte and the Whatman glass fiber separator.[134]

3.3.1 Zn^{2+}-dominated storage mechanism. The reversible (de-)intercalation process of Zn^{2+} occurs in HATP-based COFs through coordination with adjacent active sites or with intermolecular adjacent functional groups. Alshareef *et al.* reported the synthesis of a hexagonal 2D PA-COF through a solvothermal condensation reaction between CHHO and PT, employing a HATP-based COF as a cathode (Fig. 20(a)).[68] The simulated AA eclipsed model of the PA-COF aligned well with the PXRD results, confirming its periodic and well-ordered porous structure. PA-COF demonstrated a high reversible capacity (247 mA h g^{-1} at 0.1 A g^{-1}), excellent rate capability (68 mA h g^{-1} at 10 A g^{-1}) and long cycling stability with only 0.38% capacity decay per cycle over 10 000 cycles at 1.0 A g^{-1} (Fig. 20(b)). Distinctive variations at 16.2° and 24.3° observed in the *in situ* XRD patterns during cycling confirmed the formation of $Zn_4(OH)_6SO_4{\cdot}5H_2O$ (Fig. 20(c)), which was further supported by the SEM results and elemental mapping images. To explore capacity contribution, they measured capacity in pure 1.0 M $ZnSO_4$ and H_2SO_4 (pH = 5) electrolytes, revealing that the intercalation of Zn^{2+} accounted for 59.3%, 63.3%, and 66% in the first three cycles, respectively. These findings were consistent with the inductively coupled plasma atomic

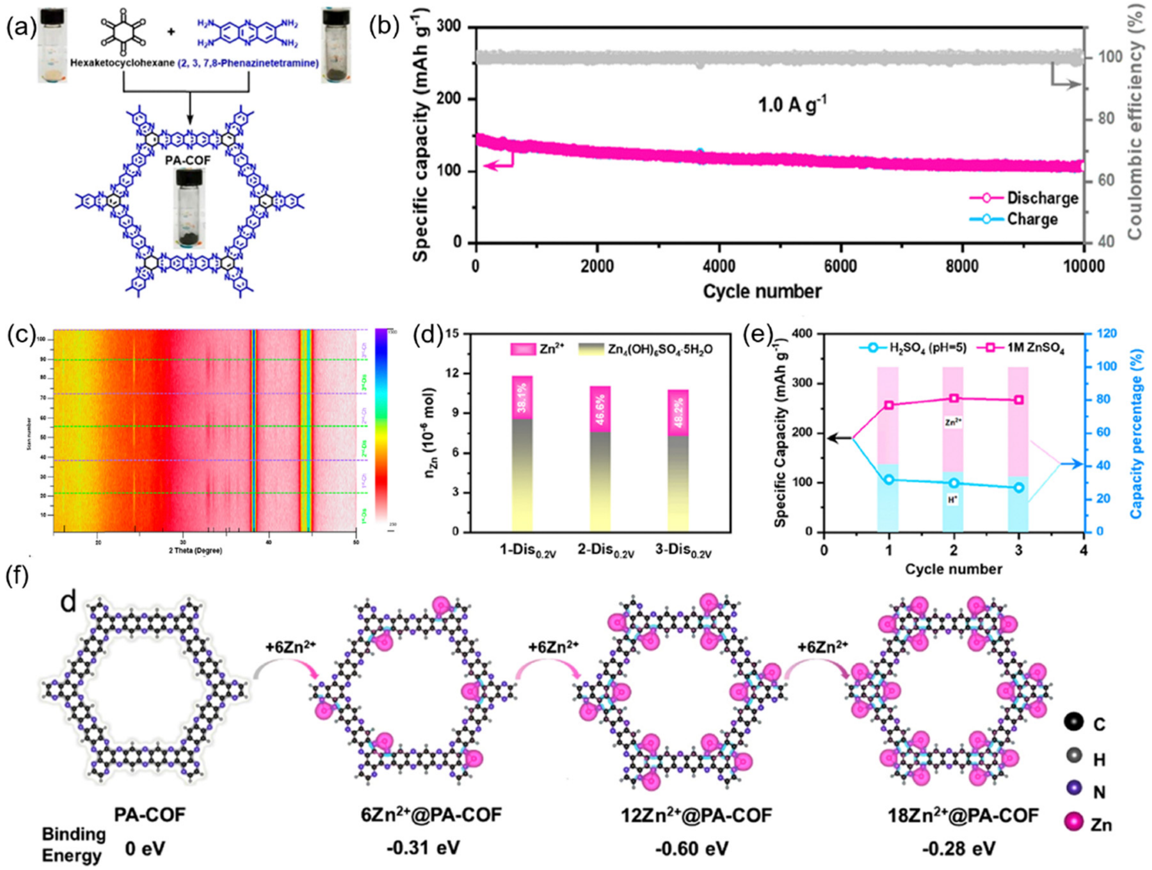

Fig. 20 (a) Synthetic route for the preparation of PA-COF. (b) Cycling performance of PA-COF at 1.0 A g^{-1}. (c) *In situ* XRD patterns of PA-COF during the first three cycles. (d) Zinc percentage calculated from Zn^{2+} and $Zn_4(OH)_6SO_4{\cdot}5H_2O$. (e) Quantitative capacity contribution of Zn^{2+} and H^+. (f) Simulated binding energies with different quantities of Zn^{2+} in PA-COF. Reproduced with permission.[68] Copyright 2020, American Chemical Society.

emission spectroscopy (ICP-AES) results (Fig. 20(d) and (e)), validating the dominant role of Zn^{2+} intercalation in the electrochemical process.

The calculated binding energies of PA-COF bonded with different quantities of Zn^{2+}—specifically 6, 12, and 18 Zn^{2+}—were all negative, which signified that the interactions between the PA-COF and Zn^{2+} were thermodynamically favorable, and reflected the strong affinity of the PA-COF for Zn^{2+} (Fig. 20(f)). Building on this work, the same group extended the research by investigating the role of different organic building blocks of HATP-based COFs—specifically benzene rings and benzoquinone units—to understand their influence on the electrochemical performance and storage mechanism of AZIBs.[121] The introduction of quinone-functional groups into the COF structure significantly enhanced the uptake capacity of Zn^{2+} and H^+, outperforming the non-quinone-functionalized cathodes. Additionally, the presence of redox-active quinone groups served as favorable binding sites for Zn^{2+}, promoting the formation of $O\cdots Zn\cdots N$ coordination. This interaction not only stabilized Zn^{2+} within the framework but also favored the competitive intercalation of Zn^{2+} over H^+, achieving high reversible capacity (339 mA h g^{-1} at 0.1 A g^{-1}) and long cycling stability (128 mA h g^{-1} after 10 000 cycles at 5 A g^{-1}).

The linkage of HATP units played a pivotal role to modulate the accessibility and activity of redox-active sites. Yu *et al.* investigated this structure–activity relationship by synthesizing two distinct HATP-based COFs through polycondensation of CHHO with PT or dibenzo[*b*,*e*][1,4]dioxine-2,3,7,8-tetraamine (Dio-4NH_2), constructing pyrazine-bridged P-HATN and dioxin-bridged D-HATN, respectively.[122] Mulliken population analysis of orbital compositions revealed a remarkable enhanced redox activity for N atoms in D-HATN, with each active N atom contributing 10.0% to the total LUMO—nearly triple the 3.8% contribution observed in P-HATN. Furthermore, D-HATN exhibited significantly attenuated π–π stacking interactions compared to P-HATN as evidenced by reduced density gradient analyses. P-HATN maintained near-planar geometry (dihedral angle of 179.75°) due to its aromaticity, while D-HATN adopted a slightly distorted configuration (dihedral angle of 174.87°) enabled by the flexible dioxin linkage. The synergistic combination of enhanced π-electron density localization at N active sites, optimized LUMO distribution, and molecular flexibility to prevent interlayer stacking collectively endowed D-HATN with higher redox-active site utilization and reversible capacity (166 mA h g^{-1} at 1 A g^{-1}) compared to P-HATN. D-HATN also achieved good cyclability, maintaining 42.2% capacity retention after 10 000 cycles at 5 A g^{-1}.

The use of *in situ* polymerization as a strategy to enhance the overall electrochemical performance of AZIBs is still considered to be effective. Zhu *et al.* initially proposed the *in situ* polymerization method in AZIBs, involving the polymerization of HATN units with dual thioether bonds on CNT substrates.[135] Notably, this approach led to a remarkable increase in capacity, from 168 mA h g^{-1} to 328 mA h g^{-1}, which was attributed to the creation of larger pore sizes and improved conductivity. The material exhibited exceptional cycling stability, retaining over 76% of its initial capacity after the extensive number of 10 000 cycles at a high current density of 20 A g^{-1}, underscoring its structural integrity and electrochemical robustness. It was evident from the CV and GCD measurements that the contribution of H^+ to the overall capacity was quantified at 10.07% in a 2 M $ZnSO_4$ electrolyte. These findings highlight the potential of *in situ* polymerization as a powerful strategy for optimizing the performance of AZIBs.

3.3.2 H^+-dominated storage mechanism.

Due to its smaller ionic radius and higher mobility, H^+ facilitates faster kinetics for proton insertion and extraction compared to the larger and slower-diffusing Zn^{2+}. The dominance of H^+-related charge storage not only improves the cycling rate but also enhances the overall power density of the batteries, making it an essential consideration for optimizing electrochemical performance of AZIBs.

Shen *et al.*'s work on HATP-based COFs represents a notable example of efforts to enhance redox activity and H^+ storage mechanisms.[123] The synthesis began with bromine-functionalized HATN-3Br; these electronegative Br atoms are highly susceptible to nucleophilic attack, making them ideal for substitution reactions. Two amino precursors, 2,6-diaminoanthracene (DA) and DAAQ, were employed as nucleophiles to two distinct COFs: DA-HATN COF and DAQ-HATN COF, respectively (Fig. 21(a)). These materials exhibited distinct electronic properties, redox activity, and structural characteristics, primarily influenced by the incorporated C═O groups. However, both DA-HATN COF and DAQ-HATN COF were relatively dense, with small micropores which could impede efficient ion diffusion and limit the accessibility of redox-active sites.

To address these limitations, rGO was introduced using a post-hydrothermal method to create larger porous networks and improve conductivity, yielding materials donated as GDA and GDAQ, respectively. The incorporation of redox-active carbonyl groups with electron-withdrawing properties into GDAQ significantly improved its electrochemical properties compared to GDA. This modification enabled GDAQ cathode to achieve a higher capacity (331 mA h g^{-1} at 0.1 A g^{-1}) with a higher plateau voltage of 0.66 V and excellent rate capability (207 mA h g^{-1} at 15 A g^{-1}). The use of X-ray photoelectron spectra (XPS) to investigate the evolution of active groups in the GDAQ cathode during the charge/discharge cycles provided valuable insight into the electrochemical processes. The XPS spectra of the discharged state of the DAQ-HATN COF revealed a noticeable reduction in the intensity of peaks assigned to the C═N and C═O bonds, which were transformed into C–N and C–O bonds, respectively (Fig. 21(b)). Upon recharging, these changes reversed, confirming the involvement of the C═O and C═N groups in electron transfer during charge storage. The emergence of N–H and O–H bonds indicated that H^+ were anchoring to the redox-active C═N and C═O sites during the discharge cycle. This was consistent with the reversible formation and disappearance of characteristic peaks for $Zn_4(OH)_6SO_4\cdot nH_2O$ (ZOHS) in *ex situ* XRD spectra (Fig. 21(c)) and the appearance of 2D flakes in SEM images (Fig. 21(d)).

By integrating the DFT calculations based on thermodynamic laws with the ICP-OES results, a detailed step-by-step mechanism for the coordination reaction involving Zn^{2+} and H^+ ions was developed. This stepwise mechanism begins with the

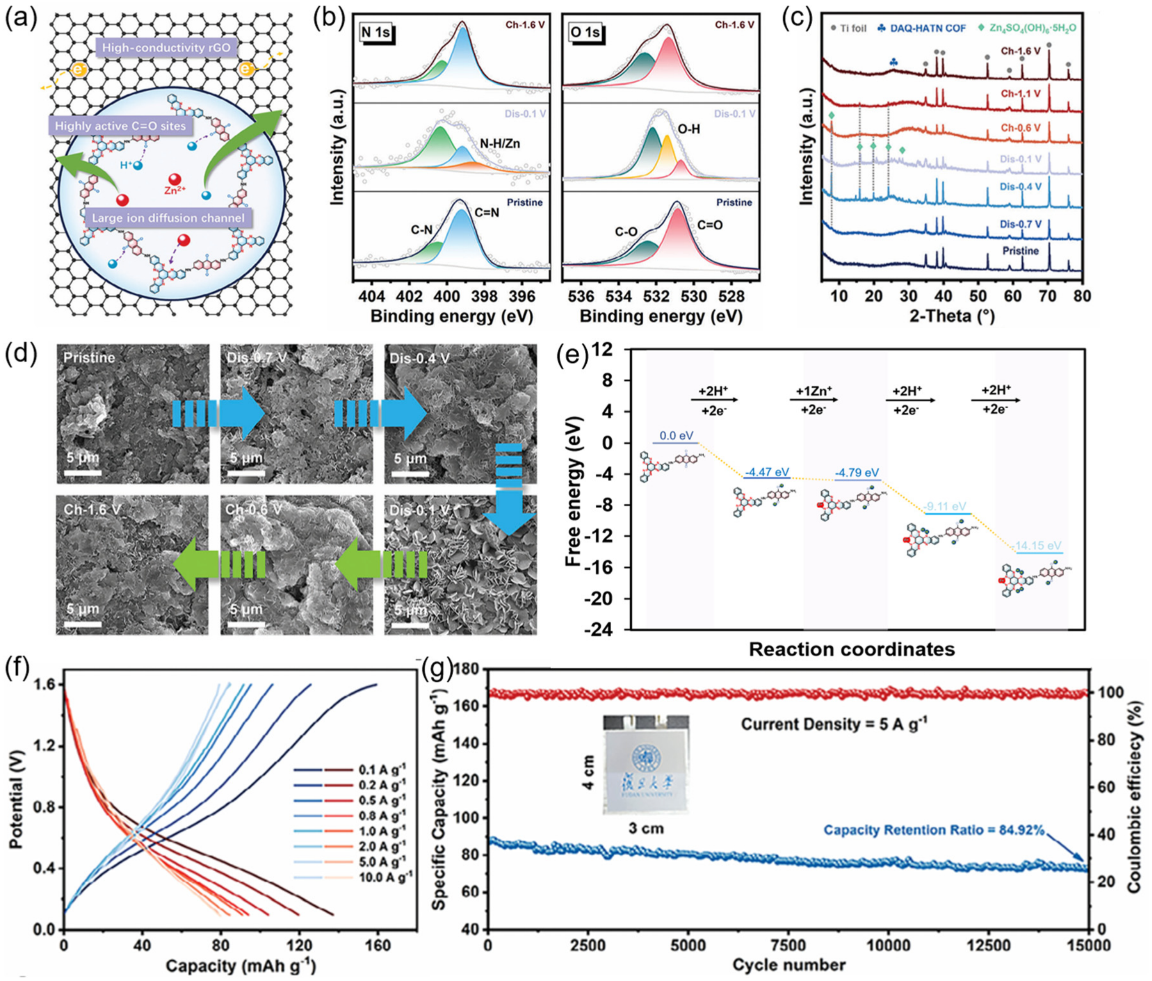

Fig. 21 (a) Structure and mechanism of GDAQ. (b) *Ex situ* XPS spectra. (c) *Ex situ* XRD patterns. (d) *Ex situ* SEM images. (e) Calculated Gibbs free energy of DAQ-HATN COF during stepped H^+/Zn^{2+} coordination process. (f) Rate performance of GDAQ//GDAQ-R pouch cells. (g) Cycling stability at 5 A g^{-1} of GDAQ//GDAQ-R pouch cells. Reproduced with permission.[123] Copyright 2024, Wiley-VCH GmbH.

C═O group coordinating with 2 H^+, followed by the coordination of Zn^{2+} with C═N groups, and finally, the protonation of the C═N group by 4 H^+ (Fig. 21(e)). The above comprehensive characterization demonstrated that the incorporation of

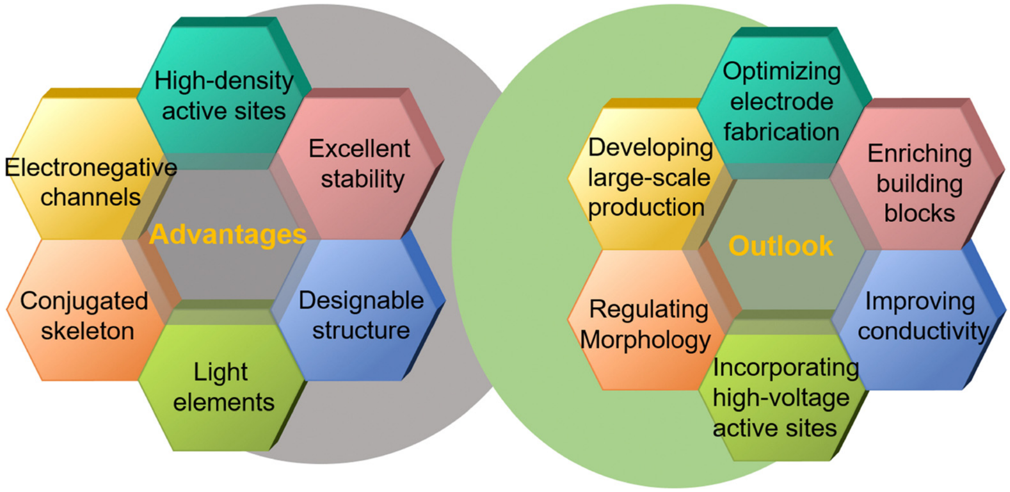

Fig. 22 Advantages and outlook of HATP-based COFs electrodes.

anthraquinone units in the DAQ-HATN COF significantly enhanced the H^+ storage capability over Zn^{2+} and elevated the average (dis-)charge potential. Building on these findings, they developed symmetric all-COF/graphene AZIBs (GDAQ//GDAQ-R) based on GDAQ as a cathode material and the reduced product of GDAQ (GDAQ-R) as an anode material. The symmetric pouch cells also demonstrated impressive rate performance (80 mA h g^{-1} at 10 A g^{-1}) and cycling stability, retaining 84.92% capacity after 2000 cycles at a high current density of 5 A g^{-1} (Fig. 21(f) and (g)).

4. Conclusions and outlook

Organic electrode materials, particularly π-conjugated HATP-based COFs, have emerged as promising alternatives to conventional inorganic options. Their highly designable structures, electronegative channels, high-density redox-active sites, excellent stability, conjugated structure, and light elements make them ideal for use in rechargeable batteries such as LIBs, SIBs, PIBs, and AZIBs (Fig. 22). In this review, we provided a summary of key research developments, ongoing challenges, and innovative strategies for structural optimization and performance enhancement. We systematically summarized the synthetic strategies for HATP-based COFs, which can be categorized into direct one-step synthesis and indirect multi-step approaches. The former enables efficient fabrication of HATP-based COFs, while the latter facilitates the construction of more diversified architectures with versatile dynamic covalent linkages, such as imine, imide, phenylimino, and triazine. Special attention was given to the unique advantages and the engineering of redox mechanisms of HATP-based COF electrodes in LIBs, specifically addressing challenges, such as insufficient and buried redox-active sites and limited electronic conductivity, while exploring potential solutions to overcome these limitations, including the incorporation of a conductive carbon matrix and the optimization of chemical structure. Furthermore, the review covered the applications of HATP-based COFs in SIBs, PIBs, and AZIBs, highlighting the exceptional adaptability and versatility of these materials across distinct electrochemical energy storage systems.

While considerable progress has been made, substantial ongoing research efforts are still imperative to simultaneously achieve high energy density and power density, including expanding structural diversity, optimizing molecular engineering and synthesis, enhancing conductivity, precisely controlling morphology, developing large-scale production, and refining electrode preparation and characterization (Fig. 23). Overcoming these challenges is crucial to unlock the full potential of HATP-based COFs in next-generation sustainable and high-performance rechargeable batteries.

4.1 Enrichment of functional building blocks

Currently, two primary methods are employed to fabricate HATP-based COFs: the direct one-step method and the indirect step-by-step method. While both have distinct advantages, expanding the range of functional building blocks and organic linkers is crucial to diversifying the structures and properties of HATP-based COFs. Although the one-step method is straightforward and efficient, improving its versatility for producing diverse HATP-based COFs remains a challenge, particularly due to the limited range of amino-functionalized organic linkers. Expanding these linkers, such as incorporating heteroatoms like S, P, or B, can enhance the electronic properties and

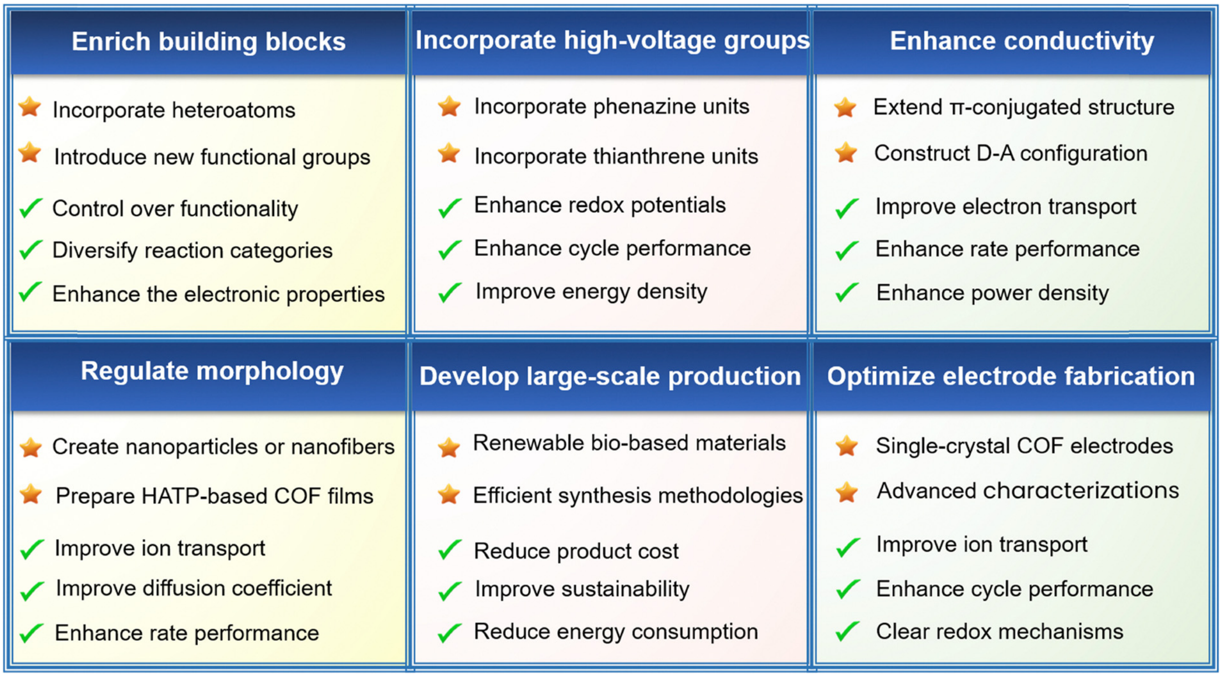

Enrich building blocks
- ★ Incorporate heteroatoms
- ★ Introduce new functional groups
- ✓ Control over functionality
- ✓ Diversify reaction categories
- ✓ Enhance the electronic properties

Incorporate high-voltage groups
- ★ Incorporate phenazine units
- ★ Incorporate thianthrene units
- ✓ Enhance redox potentials
- ✓ Enhance cycle performance
- ✓ Improve energy density

Enhance conductivity
- ★ Extend π-conjugated structure
- ★ Construct D-A configuration
- ✓ Improve electron transport
- ✓ Enhance rate performance
- ✓ Enhance power density

Regulate morphology
- ★ Create nanoparticles or nanofibers
- ★ Prepare HATP-based COF films
- ✓ Improve ion transport
- ✓ Improve diffusion coefficient
- ✓ Enhance rate performance

Develop large-scale production
- ★ Renewable bio-based materials
- ★ Efficient synthesis methodologies
- ✓ Reduce product cost
- ✓ Improve sustainability
- ✓ Reduce energy consumption

Optimize electrode fabrication
- ★ Single-crystal COF electrodes
- ★ Advanced characterizations
- ✓ Improve ion transport
- ✓ Enhance cycle performance
- ✓ Clear redox mechanisms

Fig. 23 Effective approaches applied in HATP-based COFs electrode materials for enhanced electrochemical performance.

stability of the COFs. The indirect method, by introducing new functional groups, offers additional diversity by incorporating various organic reactions, such as Debus Radziszewski, Suzuki coupling, and Yamamoto coupling reactions. Post-modification strategies could further enhance COF structure, properties, and electrochemical performance, allowing for fine-tuned control over functionality and stability.

4.2 Incorporation of high-voltage redox-active groups

Most of the HATP-based COFs used as cathode materials are primarily materials involving n-type C═N groups with (dis-)charge voltages below 3 V. To further enhance the energy density of these materials, strategic molecular engineering approaches can be developed, focusing on the incorporation of high-voltage redox-active units with operating potentials exceeding 3 V. Particularly, phenazine, phenothiazine, phenoxazine and thianthrene units with higher redox voltages and strong redox activity can be incorporated into the COFs skeleton, leading to not only higher redox potentials but also excellent electrochemical stability, thereby improving energy density.

4.3 Enhancement of conductivity

A major challenge for HATP-based COF electrodes is their poor intrinsic electrical conductivity, which limits reversible capacity and rate performance. Traditional methods, such as adding conductive agents, can increase conductivity but often reduce the content of active materials in the electrodes, negatively affecting the energy density and overall battery performance. To address this challenge, constructing HATP-based COFs with low bandgap is an effective strategy. The strategic alternation of electron-rich units and electron-deficient moieties within a donor–acceptor (D–A) configuration induces substantial bandgap narrowing, facilitating intramolecular charge transfer. Moreover, the extension of π-conjugated systems through molecular engineering facilitates electron delocalization across the framework *via* enhanced π–π orbital interactions, driven by resonance stabilization effects, acquiring high conductivity and fast charge/discharge states while preserving redox-active sites. These approaches improve charge separation, delocalization, and electron transport, essential for enhancing battery performance.

4.4 Regulation of morphology

The dense stacking of 2D HATP-based COFs into bulk structures can hinder electrochemical performance by restricting the accessibility of redox-active sites and electrolyte penetration. To maximize the exposure of redox-active sites, designing open, porous structures with well-defined channels is crucial, to facilitate ion diffusion and electrolyte interaction. Controlling COF morphology at the microscale or nanoscale—such as creating nanoparticles or nanofibers—can improve surface area and shorten ion transport paths. The integration of stereoscopic building blocks to construct 3D COFs enables the formation of interconnected hierarchical pore structures combining microporosity and mesoporosity, which offer a balance between charge storage and fast ion diffusion, enhancing both specific capacity and rate performance. These synergistic effects simultaneously enhance the accessibility of redox-active sites and charge carrier dynamics, addressing the traditional trade-off between structural stability and accessibility in 2D HATP-based COFs.

Furthermore, the development of HATP-based COF films also represents a significant advancement, offering ordered pore channels, uniform surface morphology, and distinct interfacial properties that can enhance metal-ion diffusion. HATP-based COF films can be prepared using a home-made Π-shaped PTFE holder with a SiO_2 substrate to prevent powder contamination, with the entire reaction vessel sealed in a stainless steel autoclave under identical reaction conditions to powder preparation. Notably, the optimized prepare methods enable precise control over free-standing COF film electrodes, achieving tunable thickness, reduced surface roughness, and uniform morphology. Binder-free HATP-based COF films can also effectively minimize the grain boundary effect of bulk COFs while maintaining robust structure, potentially achieving simultaneous optimization of both ionic and electronic transport.

4.5 Developing large-scale production

Despite promising laboratory-scale performance, the commercialization of HATP-based COFs still involves significant challenges, primarily the high cost of raw materials. Many organic linkers and functional groups used in COF synthesis are expensive, and their availability can be limited. Developing alternative, cheaper precursors—such as renewable bio-based or waste-derived materials—could lower production costs and improve sustainability. Additionally, parallel efforts are focused on developing more efficient synthesis methodologies. Microwave-assisted synthesis, ultrasonic-assisted synthesis, and mechanical ball milling under ambient conditions can reduce energy consumption, shorten production times, and enhance COF synthesis efficiency. However, solvothermal methods remain the most commonly used approach, and diversifying synthesis techniques could enhance electrochemical properties and enable large-scale production. These combined advancements in precursor selection and synthesis optimization are essential to bridging the gap between laboratory-scale innovation and the industrial-scale implementation of HATP-based COFs electrodes.

4.6 Optimizing electrode preparation and characterization methods

In conventional electrode preparation processes, current methods typically use HATP-based COF powders as active materials, which can result in structural heterogeneity and inconsistent particle morphologies. The development of single-crystal COF electrodes represents a transformative approach, which could offer higher crystallinity, uniform structures, and consistent molecular sizes, improving ion transport and overall electrode performance. Additionally, traditional slurry-casting methods often introduce non-conductive polymeric binders, such as polyvinylidene difluoride and polytetrafluoroethylene, hindering electron conduction and limiting electrochemical performance. The transition from non-conductive binders to conductive alternatives, such as PEDOT:PSS, can not only provide the necessary binding properties but also facilitate electron transport within the electrode, thereby enhancing overall electrochemical performance.

For characterizing electrode behavior during discharge/charge cycles, advanced techniques such as *in situ* FT-IR, PXRD, XPS, and DFT calculations are valuable, but methods like *in situ* AFM could provide real-time insights into the electrode/electrolyte interface, mechanical properties, and morphological changes, enabling more targeted improvements in electrode design. Additionally, *ex situ* solid-state NMR spectroscopy can be exploited to detect specific redox reactions involving electrolytes in HATP-based COF electrodes, particularly by visualizing structural changes intuitively through colour-mapped profiles of solid-state NMR spectra.

In short, the development of high-performance HATP-based COF electrode materials necessitates a multifaceted approach combining precision synthesis protocols, molecular structural engineering, and advanced characterization methodologies. This synergistic integration enables the rational design of optimized electrodes that simultaneously achieve enhanced energy density, excellent cycling stability, environmental friendliness and cost-effectiveness.

The exceptional electrochemical properties of HATP-based COFs that enable their outstanding electrode performance also afford them uniquely suitable for addressing various challenges in rechargeable batteries. Their characteristic periodic arrangement of HATP units and well-defined nanochannels proves equally valuable for metal anode protection, where the high-density and electronegative sites within uniform 1D channels simultaneously guide homogeneous metal deposition, suppress dendrite growth, and promote the formation of solid electrolyte interphase during repeated plating/stripping cycles. The rational molecular design of HATP-based COFs allows optimization of these protective functions across various metal anodes, including Li, Zn, Na, and Mg, while maintaining exceptional structural stability during the prolonged cycling. Furthermore, this multifunctional adaptability of HATP-based COFs can also extend to sulfur host materials in lithium sulfur batteries (LSBs). The matched redox potential between HATP-based COFs and sulfur reveals their potential as Li_2S_x reactive-type hosts, enabling efficient transformation into nanostructured Li_2S and S within the porous frameworks.

This review highlights HATP-based COFs as advanced and highly promising candidates for electrode materials in various rechargeable batteries, based on the precise tuning of their structural, electronic, and chemical properties. By leveraging this design flexibility, researchers can exploit structure–property relationships to develop electrode materials with high energy densities, excellent cycling stability, and superior safety—critical factors for the commercialization of next-generation rechargeable batteries. While HATP-based COF electrode materials face challenges across diverse metal-ion batteries, the general molecular and structural-modification strategies are valid to achieve excellent electrochemical performance. With ongoing advancements and interdisciplinary research, the application of HATP-based COFs in batteries is poised to make a significant contribution to addressing the global energy crisis, positioning them as key materials for sustainable energy solutions in the future. The accelerating pace of research in this field is sure to lead to breakthroughs that will help meet the growing demand for high-performance, safe, and cost-effective energy storage technologies.

Data availability

No primary research results, software or code have been included and no new data were generated or analysed as part of this review.

Conflicts of interest

There are no conflicts to declare.

Acknowledgements

This work was supported by the National Research Foundation (NRF) of Korea (RS-2023-00221668, RS-2024-00435493, RS-2024-00466616).

References

1 T. Hosaka, K. Kubota, A. S. Hameed and S. Komaba, *Chem. Rev.*, 2020, **120**, 6358–6466.
2 S. Haldar, A. Schneemann and S. Kaskel, *J. Am. Chem. Soc.*, 2023, **145**, 13494–13513.
3 M. Li, J. Lu, Z. Chen and K. Amine, *Adv. Mater.*, 2018, **30**, 1800561.
4 Z. Li, Y.-X. Yao, S. Sun, C.-B. Jin, N. Yao, C. Yan and Q. Zhang, *Angew. Chem., Int. Ed.*, 2023, **62**, e202303888.
5 J. Wang, Y.-F. Zhu, Y. Su, J.-X. Guo, S. Chen, H.-K. Liu, S.-X. Dou, S.-L. Chou and Y. Xiao, *Chem. Soc. Rev.*, 2024, **53**, 4230–4301.
6 L. Wang, J. Wang, Y. Lu, S. Fang, C. Yang, X. Wu, Y. Xiao, Y. Wang, S. Chou and S. Chen, *Chem. Soc. Rev.*, 2025, DOI: **10.1039/d3cs00911d**.
7 C. Zhao, Z. Yang, X. Zhou, Z. Hao, J. Chen, Z. Wang, X. Chen, X. Wu, L. Li, L. Li, L. Jiao and S. Chou, *Adv. Funct. Mater.*, 2024, **34**, 2303457.
8 C.-H. Jo, N. Voronina, Y.-K. Sun and S.-T. Myung, *Adv. Mater.*, 2021, **33**, 2006019.
9 L. Zhu, G. Ding, L. Xie, X. Cao, J. Liu, X. Lei and J. Ma, *Chem. Mater.*, 2019, **31**, 8582–8612.
10 T. Sun, J. Xie, W. Guo, D.-S. Li and Q. Zhang, *Adv. Energy Mater.*, 2020, **10**, 1904199.
11 Y. Xu, Y. Du, H. Chen, J. Chen, T. Ding, D. Sun, D. H. Kim, Z. Lin and X. Zhou, *Chem. Soc. Rev.*, 2024, **53**, 7202–7298.
12 H. Dong, N. Kang, L. Li, L. Li, Y. Yu and S. Chou, *Adv. Mater.*, 2024, **36**, 2311401.
13 H. Gao, A. R. Neale, Q. Zhu, M. Bahri, X. Wang, H. Yang, Y. Xu, R. Clowes, N. D. Browning, M. A. Little, L. J. Hardwick and A. I. Cooper, *J. Am. Chem. Soc.*, 2022, **144**, 9434–9442.

14 H. Dong, N. Kang, L. Li, L. Li, Y. Yu and S. Chou, *Adv. Mater.*, 2024, **36**, 2311401.

15 C. Guo, Y. Gao, S.-Q. Li, Y. Wang, X.-J. Yang, C. Zhi, H. Zhang, Y.-F. Zhu, S. Chen, S.-L. Chou, S.-X. Dou, Y. Xiao and X. Luo, *Adv. Funct. Mater.*, 2024, **34**, 2314851.

16 L. Cao, C. Wang, H. Wang, X. Xu, X. Tao, H. Tan and G. Zhu, *Angew. Chem., Int. Ed.*, 2024, **63**, e202402095.

17 J. Chu, Z. Liu, J. Yu, L. Cheng, H.-G. Wang, F. Cui and G. Zhu, *Angew. Chem., Int. Ed.*, 2024, **63**, e202314411.

18 L. Zhong, C. Wang, J. He, Z. lin, X. Yang, R. Li, S. Zhan, L. Zhao, D. Wu, H. Chen, Z. Tang, C. Zhi and H. Lv, *Adv. Mater.*, 2024, **36**, 2314050.

19 Z. Sun, C. Yang, Y. Zhang, J. Zhang, Z. Chen, J. Peng, C. Chen, H. Yao and S. Guan, *J. Colloid Interface Sci.*, 2025, **680**, 456–463.

20 M. Cheng, H. Wang, L. Cao, J. Shao, Y. He, X. Tao and G. Zhu, *ChemCatChem*, 2025, **17**, e202401141.

21 H. Wang, L. Cao, X. Tao and G. Zhu, *Angew. Chem., Int. Ed.*, 2025, e202502943.

22 Z. Sun, M. Shu, J. Li, B. Liu, H. Yao, S. Guan and Z. Sun, *J. Energy Chem.*, 2023, **78**, 30–36.

23 C. S. Diercks and O. M. Yaghi, *Science*, 2017, **355**, eaal1585.

24 H. Li, Z. Zhou, T. Ma, K. Wang, H. Zhang, A. H. Alawadhi and O. M. Yaghi, *J. Am. Chem. Soc.*, 2024, **146**, 35486–35492.

25 P. J. Waller, F. Gándara and O. M. Yaghi, *Acc. Chem. Res.*, 2015, **48**, 3053–3063.

26 S. E. Neumann, J. Kwon, C. Gropp, L. Ma, R. Giovine, T. Ma, N. Hanikel, K. Wang, T. Chen, S. Jagani, R. O. Ritchie, T. Xu and O. M. Yaghi, *Science*, 2024, **383**, 1337–1343.

27 K. Geng, T. He, R. Liu, S. Dalapati, K. T. Tan, Z. Li, S. Tao, Y. Gong, Q. Jiang and D. Jiang, *Chem. Rev.*, 2020, **120**, 8814–8933.

28 Y. Li, W. Chen, G. Xing, D. Jiang and L. Chen, *Chem. Soc. Rev.*, 2020, **49**, 2852–2868.

29 Q. Yan, S. Tan, R. Liu, Y. Zhi and D. Jiang, *Angew. Chem., Int. Ed.*, 2024, **63**, e202316092.

30 R. Liu, K. T. Tan, Y. Gong, Y. Chen, Z. Li, S. Xie, T. He, Z. Lu, H. Yang and D. Jiang, *Chem. Soc. Rev.*, 2021, **50**, 120–242.

31 S.-Y. Ding and W. Wang, *Chem. Soc. Rev.*, 2013, **42**, 548–568.

32 W. Wang, W. Zhao, H. Xu, S. Liu, W. Huang and Q. Zhao, *Coord. Chem. Rev.*, 2021, **429**, 213616.

33 C. Niu, S. Zhao and Y. Xu, *J. Am. Chem. Soc.*, 2024, **146**, 3114–3124.

34 A. R. Camargo, K. Endo and B. V. Lotsch, *Angew. Chem., Int. Ed.*, 2024, **63**, e202413096.

35 T. He and Y. Zhao, *Angew. Chem., Int. Ed.*, 2023, **62**, e202303086.

36 Q. Guan, L.-L. Zhou and Y.-B. Dong, *J. Am. Chem. Soc.*, 2023, **145**, 1475–1496.

37 D. W. Burke, Z. Jiang, A. G. Livingston and W. R. Dichtel, *Adv. Mater.*, 2024, **36**, 2300525.

38 F. Hu, Z. Hu, Y. Liu, K. C. Tam, R. Liang, Q. Xie, Z. Fan, C. Pan, J. Tang, G. Yu and W. Zhang, *J. Am. Chem. Soc.*, 2023, **145**, 27718–27727.

39 L. Liu, Y. Gong, Y. Tong, H. Tian, X. Wang, Y. Hu, S. Huang, W. Huang, S. Sharma, J. Cui, Y. Jin, W. Gong and W. Zhang, *CCS Chem.*, 2024, **6**, 1255–1263.

40 J. Cheng, Y. Wu, W. Zhang, J. Zhang, L. Wang, M. Zhou, F. Fan, X. Wu and H. Xu, *Adv. Mater.*, 2024, **36**, 2305313.

41 L. Qin, C. Ma, J. Zhang and T. Zhou, *Adv. Funct. Mater.*, 2024, **34**, 2401562.

42 Q. Zheng, A. Ren, A. Zagalskaya, H. Mao, D. Lee, C. Yang, K. C. Bustillo, L. F. Wan, T. A. Pham, J. A. Reimer, J. Zhang, Y. Liu and H. Zheng, *J. Am. Chem. Soc.*, 2024, **146**, 34167–34175.

43 F. Jin, H. L. Nguyen, Z. Zhong, X. Han, C. Zhu, X. Pei, Y. Ma and O. M. Yaghi, *J. Am. Chem. Soc.*, 2022, **144**, 1539–1544.

44 X. Wang, T. Fellowes, M. Bahri, H. Qu, B. Li, H. Niu, N. D. Browning, W. Zhang, J. W. Ward and A. I. Cooper, *J. Am. Chem. Soc.*, 2024, **146**, 14128–14135.

45 L. Deng, W. Chen, G. Zhou, Y. Liu, L. Liu, Y. Han, Z. Huang and D. Jiang, *J. Am. Chem. Soc.*, 2024, **146**, 35427–35437.

46 S. Ge, K. Wei, W. Peng, R. Huang, E. Akinlabi, H. Xia, M. W. Shahzad, X. Zhang, B. B. Xu and J. Jiang, *Chem. Soc. Rev.*, 2024, **53**, 11259–11302.

47 C. Sun, D. Sheng, B. Wang and X. Feng, *Angew. Chem., Int. Ed.*, 2023, **62**, e202303378.

48 C. Wang, Z. Lv, W. Yang, X. Feng and B. Wang, *Chem. Soc. Rev.*, 2023, **52**, 1382–1427.

49 Z. Xiong, L. Gu, Y. Liu, H. Wang, L. Shi, X. Wu, L. Liu and Z. Chen, *CCS Chem.*, 2024, **6**, 2835–2844.

50 H. Zhang, Z. Lin, P. Kidkhunthod and J. Guo, *Angew. Chem., Int. Ed.*, 2023, **62**, e202217527.

51 S.-Y. Ding and W. Wang, *Chem. Soc. Rev.*, 2013, **42**, 548–568.

52 M. S. Lohse and T. Bein, *Adv. Funct. Mater.*, 2018, **28**, 1705553.

53 J. Li, X. Jing, Q. Li, S. Li, X. Gao, X. Feng and B. Wang, *Chem. Soc. Rev.*, 2020, **49**, 3565–3604.

54 Z. Chen, K. Wang, Y. Tang, L. Li, X. Hu, M. Han, Z. Guo, H. Zhan and B. Chen, *Angew. Chem., Int. Ed.*, 2023, **62**, e202213268.

55 S. Kandambeth, K. Dey and R. Banerjee, *J. Am. Chem. Soc.*, 2019, **141**, 1807–1822.

56 F. Chen, H. Zheng, Y. Yusran, H. Li, S. Qiu and Q. Fang, *Chem. Soc. Rev.*, 2025, **54**, 484–514.

57 M. Yuan, F. Ma, X. Dai, L. Chen, F. Zhai, L. He, M. Zhang, J. Chen, J. Shu, X. Wang, X. Wang, Y. Zhang, X. Fu, Z. Li, C. Guo, L. Chen, Z. Chai and S. Wang, *Angew. Chem., Int. Ed.*, 2021, **60**, 21250–21255.

58 Y. Wang, J. Wang, J. Peng, Y. Jiang, Y. Zhu and Y. Yang, *ACS Nano*, 2024, **18**, 23958–23967.

59 F. Xu, S. Jin, H. Zhong, D. Wu, X. Yang, X. Chen, H. Wei, R. Fu and D. Jiang, *Sci. Rep.*, 2015, **5**, 8225.

60 B. Sun, Z. Sun, Y. Yang, X. L. Huang, S. C. Jun, C. Zhao, J. Xue, S. Liu, H. K. Liu and S. X. Dou, *ACS Nano*, 2024, **18**, 28–66.

61 L. Cheng, X. Yan, J. Yu, X. Zhang, H.-G. Wang, F. Cui and Y. Wang, *Adv. Mater.*, 2025, **37**, 2411625.

62 X.-X. Luo, W.-H. Li, H.-J. Liang, H.-X. Zhang, K.-D. Du, X.-T. Wang, X.-F. Liu, J.-P. Zhang and X.-L. Wu, *Angew. Chem., Int. Ed.*, 2022, **61**, e202117661.

63 J. Lee, H. Lim, J. Park, M.-S. Kim, J.-W. Jung, J. Kim and I.-D. Kim, *Adv. Energy Mater.*, 2023, **13**, 2300442.

64 H. Li, M. Cao, Z. Fu, Q. Ma, L. Zhang, R. Wang, F. Liang, T. Zhou and C. Zhang, *Chem. Sci.*, 2024, **15**, 4341–4348.

65 S. Zheng, D. Shi, D. Yan, Q. Wang, T. Sun, T. Ma, L. Li, D. He, Z. Tao and J. Chen, *Angew. Chem., Int. Ed.*, 2022, **61**, e202117511.

66 D. Ma, H. Zhao, F. Cao, H. Zhao, J. Li, L. Wang and K. Liu, *Chem. Sci.*, 2022, **13**, 2385–2390.

67 D. Luo, J. Zhang, H. Zhao, H. Xu, X. Dong, L. Wu, B. Ding, H. Dou and X. Zhang, *Chem. Commun.*, 2023, **59**, 6853–6856.

68 W. Wang, V. S. Kale, Z. Cao, S. Kandambeth, W. Zhang, J. Ming, P. T. Parvatkar, E. A. Hamad, O. Shekhah, L. Cavallo, M. Eddaoudi and H. N. Alshareef, *ACS Energy Lett.*, 2020, **5**, 2256–2264.

69 J. Wang, X. Zhang, Z. Liu, J. Yu, H.-G. Wang, X.-L. Wu, F. Cui and G. Zhu, *Angew. Chem., Int. Ed.*, 2024, **63**, e202401559.

70 Z. Sun, H. Yao, J. Li, B. Liu, Z. Lin, M. Shu, H. Liu, S. Zhu and S. Guan, *ACS Appl. Mater. Interfaces*, 2023, **15**, 42603–42610.

71 Z. Tian, V. S. Kale, Z. Shi, J. Yin, S. Kandambeth, Y. Wang, A.-H. Emwas, Y. Lei, X. Guo, J. Ming, W. Wang, N. Alsadun, O. Shekhah, M. Eddaoudi and H. N. Alshareef, *ACS Nano*, 2023, **17**, 13961–13973.

72 J. L. Segura, R. Juárez, M. Ramos and C. Seoane, *Chem. Soc. Rev.*, 2015, **44**, 6850–6885.

73 S. Kandambeth, J. Jia, H. Wu, V. S. Kale, P. T. Parvatkar, J. Czaban-Jóźwiak, S. Zhou, X. Xu, Z. O. Ameur, E. Abou-Hamad, A.-H. Emwas, O. Shekhah, H. N. Alshareef and M. Eddaoudi, *Adv. Energy Mater.*, 2020, **10**, 2001673.

74 J. Mahmood, S.-J. Kim, H.-J. Noh, S.-M. Jung, I. Ahmad, F. Li, J.-M. Seo and J.-B. Baek, *Angew. Chem., Int. Ed.*, 2018, **57**, 3415–3420.

75 S.-Q. Xu, T.-G. Zhan, Q. Wen, Z.-F. Pang and X. Zhao, *ACS Macro Lett.*, 2016, **5**, 99–102.

76 X. Liu, Y. Jin, H. Wang, X. Yang, P. Zhang, K. Wang and J. Jiang, *Adv. Mater.*, 2022, **34**, 2203605.

77 B. Yao, G. Li, X. Wu, H. Sun, X. Liu, F. Li and T. Guo, *Chem. Commun.*, 2024, **60**, 793–803.

78 L. Xu, Y. Liu, Y. Li, X. Xuan, X. Xu, Z. Gong and L. Pan, *J. Mater. Chem. A*, 2024, **12**, 29814–29825.

79 N. Tahir, G. Wang, I. Onyshchenko, N. D. Geyter, K. Leus, R. Morent and P. V. D. Voort, *J. Catal.*, 2019, **375**, 242–248.

80 J. Mahmood, E. K. Lee, M. Jung, D. Shin, I.-Y. Jeon, S.-M. Jung, H.-J. Choi, J.-M. Seo, S.-Y. Bae, S.-D. Sohn, N. Park, J. H. Oh, H.-J. Shin and J.-B. Baek, *Nat. Commun.*, 2015, **6**, 6486.

81 Z. Meng, A. Aykanat and K. A. Mirica, *Chem. Mater.*, 2019, **31**, 819–825.

82 Q. Peng, H. Dong, H. Yan, Y. Xiao, Y. Wang, S. Chou and S. Chen, *Energy Storage Mater.*, 2024, **73**, 103849.

83 X. Li, H. Wang, H. Chen, Q. Zheng, Q. Zhang, H. Mao, Y. Liu, S. Cai, B. Sun, C. Dun, M. P. Gordon, H. Zheng, J. A. Reimer, J. J. Urban, J. Ciston, T. Tan, E. M. Chan, J. Zhang and Y. Liu, *Chem*, 2020, **6**, 933–944.

84 H. Huang, Y. Zhao, Y. Bai, F. Li, Y. Zhang and Y. Chen, *Adv. Sci.*, 2020, **7**, 2000012.

85 M. Shi, R. Wang, J. He, L. Zhao, K. Dai and C. Yan, *Chem. Eng. J.*, 2022, **450**, 138238.

86 D. Zhao, Z. Li, D. Xu and Z. Yang, *Adv. Funct. Mater.*, 2024, **34**, 2316182.

87 L. M. Klivansky, D. Hanifi, G. Koshkakaryan, D. R. Holycross, E. K. Gorski, Q. Wu, M. Chai and Y. Liu, *Chem. Sci.*, 2012, **3**, 2009.

88 S.-Q. Xu, R.-R. Liang, T.-G. Zhan, Q.-Y. Qi and X. Zhao, *Chem. Commun.*, 2017, **53**, 2431–2434.

89 S. Xu, G. Wang, B. P. Biswal, M. Addicoat, S. Paasch, W. Sheng, X. Zhuang, E. Brunner, T. Heine, R. Berger and X. Feng, *Angew. Chem., Int. Ed.*, 2019, **58**, 849–853.

90 S. Xu, H. Sun, M. Addicoat, B. P. Biswal, F. He, S. W. Park, S. Paasch, T. Zhang, W. Sheng, E. Brunner, Y. Hou, M. Richter and X. Feng, *Adv. Mater.*, 2021, **33**, 2006274.

91 R. Iqbal, M. K. Majeed, A. Hussain, A. Ahmad, M. Ahmad, B. Jabar, A. R. Akbar, S. Ali, S. Rauf and A. Saleem, *Mater. Chem. Front.*, 2023, **7**, 2464–2474.

92 S. Xu, Z. Liao, A. Dianat, S.-W. Park, M. A. Addicoat, Y. Fu, D. L. Pastoetter, F. G. Fabozzi, Y. Liu, G. Cuniberti, M. Richter, S. Hecht and X. Feng, *Angew. Chem., Int. Ed.*, 2022, **61**, e202202492.

93 S. Ma, T. Deng, Z. Li, Z. Zhang, J. Jia, Q. Li, G. Wu, H. Xia, S.-W. Yang and X. Liu, *Angew. Chem., Int. Ed.*, 2022, **61**, e202208919.

94 D. L. Pastoetter, S. Xu, M. Borrelli, M. Addicoat, B. P. Biswal, S. Paasch, A. Dianat, H. Thomas, R. Berger, S. Reineke, E. Brunner, G. Cuniberti, M. Richter and X. Feng, *Angew. Chem., Int. Ed.*, 2020, **59**, 23620–23625.

95 B. Zhang, M. Wei, H. Mao, X. Pei, S. A. Alshmimri, J. A. Reimer and O. M. Yaghi, *J. Am. Chem. Soc.*, 2018, **140**, 12715–12719.

96 X. Guan, H. Li, Y. Ma, M. Xue, Q. Fang, V. Valtchev and S. Qiu, *Nat. Chem.*, 2019, **11**, 587–594.

97 Y. Yusran, Q. Fang and S. Qi, *Isr. J. Chem.*, 2018, **58**, 971–984.

98 R. Xiao, J. M. Tobin, M. Zha, Y.-L. Hou, J. He, F. Vilela and Z. Xu, *J. Mater. Chem. A*, 2017, **5**, 20180–20187.

99 S.-W. Kim, H. Jung, M. S. Okyay, H.-J. Noh, S. Chung, Y. H. Kim, J.-P. Jeon, B. M. Wong, K. Cho, J.-M. Seo, J.-W. Yoo and J.-B. Baek, *Angew. Chem., Int. Ed.*, 2023, **62**, e202310560.

100 S. Li, Y. Liu, L. Dai, S. Li, B. Wang, J. Xie and P. Li, *Energy Storage Mater.*, 2022, **48**, 439–446.

101 G. Zhao, H. Li, Z. Gao, L. Xu, Z. Mei, S. Cai, T. Liu, X. Yang, H. Guo and X. Sun, *Adv. Funct. Mater.*, 2021, **31**, 2101019.

102 H. Duan, K. Li, M. Xie, J.-M. Chen, H.-G. Zhou, X. Wu, G.-H. Ning, A. I. Cooper and D. Li, *J. Am. Chem. Soc.*, 2021, **143**, 19446–19453.

103 X. Wu, S. Zhang, X. Xu, F. Wen, H. Wang, H. Chen, X. Fan and N. Huang, *Angew. Chem., Int. Ed.*, 2024, **63**, e202319355.

104 X. Yang, L. Gong, X. Liu, P. Zhang, B. Li, D. Qi, K. Wang, F. He and J. Jiang, *Angew. Chem., Int. Ed.*, 2022, **61**, e202207043.

105 X. Yang, L. Gong, Y. Jin, T. Zheng, X. Wang, Q. Zhi, B. Yu, K. Wang and J. Jiang, *CCS Chem.*, 2025, DOI: **10.31635/ccschem.024.202405020**.

106 M. K. Shehab and H. M. El-Kaderi, *ACS Appl. Mater. Interfaces*, 2024, **16**, 14750–14758.

107 Y. Lin, H. Cui, C. Liu, R. Li, S. Wang, G. Qu, Z. Wei, Y. Yang, Y. Wang, Z. Tang, H. Li, H. Zhang, C. Zhi and H. Lv, *Angew. Chem., Int. Ed.*, 2023, **62**, e202218745.

108 C. Wang, R. Li, Y. Zhu, Y. Wang, Y. Lin, L. Zhong, H. Chen, Z. Tang, H. Li, F. Liu, C. Zhi and H. Lv, *Adv. Energy Mater.*, 2024, **14**, 2302495.

109 D. Geng, H. Zhang, Z. Fu, Z. Liu, J. Yang and C. Yan, *Energy Storage Mater.*, 2025, **75**, 103996.

110 G. Wang, N. Tahir, I. Onyshchenko, N. D. Geyter, R. Morent, K. Leus and P. V. D. Voort, *Microporous Mesoporous Mater.*, 2019, **290**, 109650.

111 X. Chen, D. Liu, C. Yang, L. Shi and F. Li, *Inorg. Chem.*, 2023, **62**, 9360–9368.

112 Z. He, T. Luan, S. Zhang, Q. Wei, D. Huang, L. Wang, Y. Wang, P. Li and W. W. Yu, *Adv. Mater.*, 2024, **36**, 2410363.

113 C. Peng, G.-H. Ning, J. Su, G. Zhong, W. Tang, B. Tian, C. Su, D. Yu, L. Zu, J. Yang, M.-F. Ng, Y.-S. Hu, Y. Yang, M. Armand and K. P. Loh, *Nat. Energy*, 2017, **2**, 17074.

114 Q. Bai, J. Huang, K. Tang, Y. Zhu and D. Wu, *Adv. Mater.*, 2025, **37**, 2416661.

115 Z. Sun, J.-M. Seo, H. Liu, Y. Wei, Y. Zhang, Z. Li, H. Yao, S. Guan and J.-B. Baek, *Nano Energy*, 2024, **129**, 110073.

116 M. Wu, Y. Zhao, B. Sun, Z. Sun, C. Li, Y. Han, L. Xu, Z. Ge, Y. Ren, M. Zhang, Q. Zhang, Y. Lu, W. Wang, Y. Ma and Y. Chen, *Nano Energy*, 2020, **70**, 104498.

117 J. Chu, L. Cheng, L. Chen, H.-G. Wang, F. Cui and G. Zhu, *Chem. Eng. J.*, 2023, **451**, 139016.

118 R. Shi, L. Liu, Y. Lu, C. Wang, Y. Li, L. Li, Z. Yan and J. Chen, *Nat. Commun.*, 2020, **11**, 178.

119 X. Yang, L. Gong, Z. Liu, Q. Zhi, B. Yu, X. Chen, K. Wang, X. Li, D. Qi and J. Jiang, *Sci. China: Chem.*, 2024, **67**, 1300–1310.

120 X.-L. Chen, M. Xie, Z.-L. Zheng, X. Luo, H. Jin, Y.-F. Chen, G.-Z. Yang, D.-S. Bin and D. Li, *J. Am. Chem. Soc.*, 2023, **145**, 5105–5113.

121 W. Wang, V. S. Kale, Z. Cao, Y. Lei, S. Kandambeth, G. Zou, Y. Zhu, E. Abouhamad, O. Shekhah, L. Cavallo, M. Eddaoudi and H. N. Alshareef, *Adv. Mater.*, 2021, **33**, 2103617.

122 L. Zhong, C. Liu, Y. Zhang, J. Li, F. Yang, Z. Zhang and D. Yu, *Angew. Chem., Int. Ed.*, 2025, **64**, e202413971.

123 P. Yi, Z. Li, L. Ma, B. Feng, Z. Liu, Y. Liu, W. Lu, S. Cao, H. Fang, M. Ye and J. Shen, *Adv. Mater.*, 2024, **36**, 2414379.

124 J. Xie, Z. Wang, Z. J. Xu and Q. Zhang, *Adv. Energy Mater.*, 2018, **8**, 1703509.

125 P. Xu, F. Gao and D. Liu, *Adv. Mater. Interfaces*, 2023, **10**, 2300464.

126 M. Mao, C. Luo, T. P. Pollard, S. Hou, T. Gao, X. Fan, C. Cui, J. Yue, Y. Tong, G. Yang, T. Deng, M. Zhang, J. Ma, L. Suo, O. Borodin and C. Wang, *Angew. Chem., Int. Ed.*, 2019, **58**, 17820–17826.

127 J. Park, M. Lee, D. Feng, Z. Huang, A. C. Hinckley, A. Yakovenko, X. Zou, Y. Cui and Z. Bao, *J. Am. Chem. Soc.*, 2018, **140**, 10315–10323.

128 Y. Hu, W. Tang, Q. Yu, X. Wang, W. Liu, J. Hu and C. Fan, *Adv. Funct. Mater.*, 2020, **30**, 2000675.

129 J. Zoua, K. Fana, X. Wang, Y. Chen, Y. Cao, H. Dai, C. Zhang, M. Fu, Y. Gao, H. Liu and C. Wang, *Chem. Eng. J.*, 2023, **460**, 141703.

130 S. Zhang, Y.-L. Zhu, S. Ren, C. Li, X.-B. Chen, Z. Li, Y. Han, Z. Shi and S. Feng, *J. Am. Chem. Soc.*, 2023, **145**, 17309–17320.

131 J. Wei, P. Zhang, J. Sun, Y. Liu, F. Li, H. Xu, R. Ye, Z. Tie, L. Sun and Z. Jin, *Chem. Soc. Rev.*, 2024, **53**, 10335–10369.

132 S. Li, J. Shang, M. Li, M. Xu, F. Zeng, H. Yin, Y. Tang, C. Han and H.-M. Cheng, *Adv. Mater.*, 2023, **35**, 2207115.

133 Y. Chen, J. Li, Q. Zhu, K. Fan, Y. Cao, G. Zhang, C. Zhang, Y. Gao, J. Zou, T. Zhai and C. Wang, *Angew. Chem., Int. Ed.*, 2022, **61**, e202116289.

134 J. Ning, X. Zhang, D. Xie, Q. He, J. Hu, J. Tang, R. Li, H. Meng and K. X. Yao, *Angew. Chem., Int. Ed.*, 2024, **63**, e202319796.

135 J. Wang, Z. Liu, H.-G. Wang, F. Cui and G. Zhu, *Chem. Eng. J.*, 2022, **450**, 138051.